JGR Oceans

RESEARCH ARTICLE
10.1029/2024JC021880

Key Points:

- Nearby major thrust-faulting and normal-faulting earthquakes of similar magnitude demonstrate source mechanism effects on tsunami characteristics
- Seismic and ocean wave modeling reveals sensitivity of near- and far-field tsunamis to faulting geometry, depth extent, and location
- Source-location dependent wave refraction over near-field bathymetric features strongly influences directionality of far-field tsunamis

Supporting Information:

Supporting Information may be found in the online version of this article.

Correspondence to:

K. F. Cheung,
cheung@hawaii.edu

Citation:

Robert, W. H., Yamazaki, Y., Cheung, K. F., & Lay, T. (2025). Tsunami variability for the 2021 megathrust and 2023 outer rise M_W 7.7 earthquakes southeast of the Loyalty Islands. *Journal of Geophysical Research: Oceans*, *130*, e2024JC021880. https://doi.org/10.1029/2024JC021880

Received 23 SEP 2024
Accepted 29 JAN 2025

Author Contributions:

Conceptualization: Kwok Fai Cheung, Thorne Lay
Data curation: William H. Robert, Yoshiki Yamazaki, Thorne Lay
Formal analysis: William H. Robert, Yoshiki Yamazaki, Thorne Lay
Funding acquisition: Kwok Fai Cheung
Investigation: William H. Robert, Yoshiki Yamazaki, Kwok Fai Cheung, Thorne Lay
Methodology: William H. Robert, Yoshiki Yamazaki, Kwok Fai Cheung, Thorne Lay
Project administration: Kwok Fai Cheung
Resources: Kwok Fai Cheung, Thorne Lay
Software: William H. Robert, Yoshiki Yamazaki, Thorne Lay
Supervision: Kwok Fai Cheung

Tsunami Variability for the 2021 Megathrust and 2023 Outer Rise M_W 7.7 Earthquakes Southeast of the Loyalty Islands

William H. Robert[1,2], Yoshiki Yamazaki[1], Kwok Fai Cheung[1], and Thorne Lay[3]

[1]Department of Ocean and Resources Engineering, University of Hawaii at Manoa, Honolulu, HI, USA, [2]Now at Stantec, Austin, TX, USA, [3]Department of Earth and Planetary Sciences, University of California Santa Cruz, Santa Cruz, CA, USA

Abstract The 2021 shallow plate-boundary thrust-faulting and 2023 outer rise normal-faulting M_W 7.7 earthquakes southeast of the Loyalty Islands produced significant, well-recorded tsunamis around the North and South Fiji Basins. The two earthquakes occurred in close proximity on opposing sides of the Southern Vanuatu Trench with similar seismic moments and east-west rupture lengths but different faulting mechanisms. This provides a basis to examine tsunami sensitivity to source geometry and location for paths in the complex southwest Pacific region. Finite-fault models of the source processes for both events were inverted from teleseismic body wave data with constraints from forward, nonhydrostatic modeling of regional tide gauge and seafloor pressure sensor recordings. The wave motions are reversed in sign, with a leading crest generated by 1.31 m uplift on the upper plate slope for the 2021 tsunami and a leading trough from 2.37 m subsidence on the subducting plate near the trench for the 2023 tsunami. The more recent outer rise normal faulting produces narrower seafloor deformation beneath deeper water resulting in shorter period tsunami waves that shoal and refract more effectively along seamounts and island chains to produce a more elaborate radiation pattern. The source location relative to seamounts and small islands in the near field influences the energy lobes and directionality of the far-field tsunami to the north. In contrast, both events have very similar radiation patterns to the south due to absence of major bathymetric features immediately southward of the sources.

Plain Language Summary The 2021 thrust-faulting and 2023 normal-faulting M_W 7.7 earthquakes on opposing sides of the Southern Vanuatu Trench southeast of the Loyalty Islands produced significant, well-recorded tsunamis around the North and South Fiji Basins. The two nearby earthquakes with similar magnitude and east-west rupture extents but different source mechanisms provide a basis to examine tsunami sensitivity to source processes for paths in the complex southwest Pacific region. Rupture and tsunami models were determined from recorded seismic and water level data for both events. The 2021 and 2023 tsunamis, respectively, have a leading crest and a leading trough generated by 1.31 m uplift on the upper plate slope and 2.37 m subsidence on the subducting plate near the trench. The 2023 earthquake has narrower seafloor deformation beneath deeper water resulting in shorter period tsunami waves that are focused more effectively along seamounts and island chains to produce a more elaborate wave pattern. The source location relative to nearby seamounts and small islands influences the direction and energy of the tsunami to the north. In contrast, both events have very similar wave patterns to the south due to the absence of major bathymetric features immediately southward of the sources.

1. Introduction

Tsunamis produced by large subduction zone earthquakes have repeatedly caused widespread casualties, extensive damage to infrastructure, and disruption of essential services both near and far from the sources. In the southwest Pacific, island nations and coastal communities are particularly vulnerable to earthquakes and tsunamis due to their isolated localities and geographic proximity to active subduction zones that generate major tsunamigenic interplate thrust-faulting earthquakes as well as outer rise normal-faulting earthquakes (e.g., Heidarzadeh et al., 2016; Roger & Pelletier, 2024). Governments, scientists, and stakeholders are motivated to understand the hazards and risks of earthquakes and tsunamis to support comprehensive risk management strategies in the region (UNESCO-IOC, 2025).

The tectonic plate margin in the Vanuatu subduction zone is notably complex. It is generally characterized by interaction between the subducting Australian plate and the overriding Pacific plate along its ~1,800 km extent

Validation: William H. Robert, Yoshiki Yamazaki, Thorne Lay
Visualization: William H. Robert, Yoshiki Yamazaki, Thorne Lay
Writing – original draft: William H. Robert
Writing – review & editing: Kwok Fai Cheung, Thorne Lay

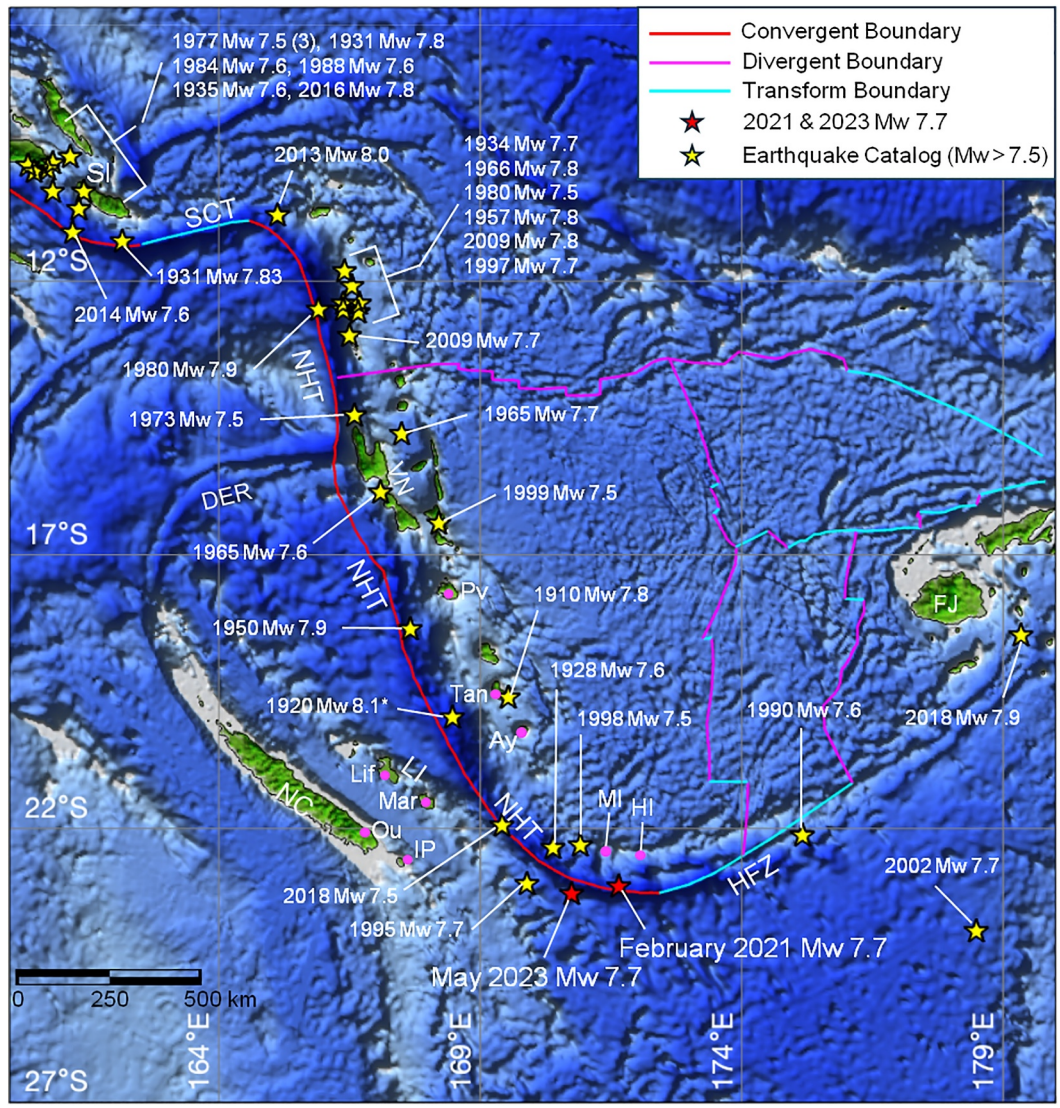

Figure 1. Historical earthquakes ($M_W \geq 7.5$) in the Vanuatu subduction zone since 1900. Abbreviations: SCT, San Cristobal Trench; NHT, New Hebrides Trench; HFZ, Hunter fracture zone; SI, Solomon Islands; VN, Vanuatu; DER, D'Entrecasteaux Ridge; LI, Loyalty Islands; NC, New Caledonia; FJ, Fiji; Pv, Port Vila; Tan, Tanna; Ay, Aneityum; Mar, Mare; IP, Isle of Pines; Lif, Lifou Island; Ou, Ouinne; MI, Matthew Island; HI, Hunter Island. Base map generated from GEBCO; plate boundaries and earthquake data from USGS. *Updated to M_W 7.5–7.8 by Ioualalen et al. (2017).

from the Solomon Islands (10°S, 165°E) to the Hunter fracture zone (23°S, 173°E), as shown in Figure 1. Along this extensive, curved plate boundary, volcanic activity has formed the Solomon Islands, Loyalty Islands, and Vanuatu Islands in distinct phases. The Solomon Archipelago has experienced an overall complex history of formation and accretion since Cretaceous times (Petterson et al., 1999). The Loyalty Islands formed from Eocene and Oligocene-Miocene volcanic arc remnants (Agranier et al., 2023; Gans et al., 2023), whereas Vanuatu volcanism originated in early to middle Miocene (Carney & Macfarlane, 1982). The relative plate movement is roughly perpendicular to the Solomon and New Hebrides Trenches, with convergence rates varying from 170 mm/yr along the Solomon Islands to 27 mm/yr near the underthrust D'Entrecasteaux Ridge as localized convergent deformation occurs on the eastern side of the Vanuatu arc (Bergeot et al., 2009). Further south, the subduction zone converges at 90–120 mm/yr and then curves eastward (Calmant et al., 2003). This appears to involve two distinct systems separated by collision of the Loyalty Ridge with the arc and divided into old eastward and very young (<2 Ma) northward subduction (e.g., Patriat et al., 2015, 2019), before transforming to a strike-slip boundary along the Hunter fracture zone. Near Matthew and Hunter Islands there is strong partitioning of the

Table 1
Summary of Source Parameters From USGS-NEIC, Global Centroid Moment Tensor, and Preferred Models in This Study for the 2021 Thrust-Faulting and 2023 Normal-Faulting M_W 7.7 Earthquakes

Earthquake	Solution	Strike (°)	Dip (°)	Rake (°)	Seismic moment (Nm)	Centroid depth (km)
2021	USGS-NEIC W-phase	246	17	65	4.364×10^{20}	25.5
	GCMT best double-couple	277	22	98	4.12×10^{20}	21.0
	Preferred finite fault model	277	5–38	95 ± 45	4.37×10^{20}	12.4
2023	USGS-NEIC W-phase	80/260	51/39	−90/−90	4.011×10^{20}	15.5
	GCMT best double-couple	66/275	46/48	−111/−70	4.30×10^{20}	20.1
	Preferred finite fault model	80	32.5	−90 ± 45	4.23×10^{20}	15.8

increasingly oblique convergence with a boundary perpendicular rate of ∼50 mm/yr and left lateral strike-slip motion of ∼90 mm/yr on a sliver fault in the upper plate along the islands (e.g., Calmant et al., 2003; Power et al., 2011).

Tsunamis in the region have been predominantly generated by earthquakes with volcanic and non-seismic sources representing less than 5% of documented events (Roger & Pelletier, 2024). The Northern Vanuatu subduction zone has produced several large earthquakes in the past century (e.g., Cleveland et al., 2014), one of the largest being the 6 February 2013 M_W 8.0 Santa Cruz Islands thrust faulting with shallow eastward dip (e.g., Lay et al., 2013). The resulting tsunami reached several villages on the Island of Nendo, where waves greater than 1 m claimed 10 lives and caused extensive damage to the town of Lata in the New Georgia Islands and the Solomon Islands (Romano et al., 2015). Several other tsunamigenic earthquakes with $M_W > 7.5$ have also been observed and most of the tsunamis were limited to the near field with notable reporting discrepancies in the Vanuatu-New Caledonia region (Roger & Pelletier, 2024). Across the d'Entrecasteaux Ridge, the Southern Vanuatu subduction zone produced 12 M_W 7.5+ earthquakes in the last century and is known for strong and long-duration aftershock sequences (Ye et al., 2021). Sahal et al. (2010) cataloged several events, in which eyewitness accounts and observational records suggest tsunami runup of 1–2.5 m at Lifou and Port Vila, with wave arrivals within 20 min to ∼1 hr of the reported earthquake origin times. At the southern hook of the subduction zone, there is still reasonable potential for tsunamigenic thrust earthquakes due to the arc-normal compression between 169° and 172°E. The region has limited historical documentation, but there is no clear evidence that $M_W \geq 8.0$ earthquakes have occurred between 170° and 175°E (Gusman et al., 2022).

The two largest earthquakes in the Southern Vanuatu subduction zone in the past quarter-century occurred in 2021 and 2023 (Table 1), with both producing tsunamis across the southwest Pacific. According to the US Geological Survey National Earthquake Information Center (USGS-NEIC), the 10 February 2021 M_W 7.7 earthquake occurred at 13:19:55 UTC with an epicenter at (23.051°S, 171.657°E) (https://earthquake.usgs.gov/earthquakes/eventpage/us6000dg77/executive). The USGS-NEIC W-phase moment tensor solution indicates a predominantly shallow-dipping thrust-faulting event for an assumed plate boundary rupture and a best double-couple mechanism with 246° strike, 17° dip, 65° rake, and a seismic moment of 4.364×10^{20} Nm (M_W 7.7) at a centroid depth of 25.5 km. In comparison, the global centroid moment tensor (GCMT) solution has the best double-couple mechanism with 277° strike, 22° dip, 98° rake, and a seismic moment of 4.12×10^{20} Nm (M_W 7.7) at a centroid depth of 21.0 km (https://www.globalcmt.org/CMTsearch.html). The largest, recorded coastal tsunami amplitude was 133.5 cm at Lenakel, Vanuatu, 56 min after the earthquake (Roger et al., 2023). The 19 May 2023 event occurred ∼95 km west-southwest of the 2021 rupture. The origin time was 02:57:03 UTC with an epicenter at (23.206°S, 170.742°E) (https://earthquake.usgs.gov/earthquakes/eventpage/us6000kd0n/executive). The USGS-NEIC W-phase solution has an extensional-faulting mechanism with 80°/260° strike, 51°/39° dip, and −90°/−90° rake, and a seismic moment of 4.011×10^{20} Nm (M_W 7.7) at a centroid depth of 15.5 km. The GCMT best double-couple solution has 66°/275° strike, 46°/48° dip, −111°/−70° rake, a seismic moment of 4.30×10^{20} Nm (M_W 7.7), and a centroid depth of 20.1 km. The event pair, which occurred on opposing sides of the Southern Vanuatu Trench within 2 years, is analogous to the 2013 M_W 8.0 Santa Cruz thrust-faulting and 2015 M_W 7.0 normal-faulting earthquakes in the Northern Vanuatu subduction zone (Heidarzadeh et al., 2016).

The polarity, amplitude, and period of tsunami waves depend on the seafloor displacement caused by the earthquake as well as the local water depth. Water-level stations with appropriate sampling rates and positioning

with respect to the source can provide reliable constraints to determine the seafloor deformation and the slip extent. Many prior studies have explored these complementary features of tsunami, seismic, and geodetic records to deduce finite fault models for major earthquakes through geophysical data inversion and tsunami forward modeling (e.g., Bai, Liu, et al., 2023; Gusman et al., 2015; Li et al., 2016; Yamazaki, Lay, et al., 2011; Yamazaki et al., 2018). Due to the lack of historical tsunami data from major earthquake sources in the southern hook of the Vanuatu subduction zone, as apparent in Figure 1, the observations for the 2021 and 2023 M_W 7.7 earthquakes provide an opportunity to consider the tsunami behavior in the southwest Pacific, which shows strong north-south wave radiation in contrast to east-west radiation of events further north that primarily impact Australia, New Caledonia, and Fiji. We implement the joint modeling approach with seismic and water-level records to determine the source models and associated tsunami wave fields for the 2021 and 2023 events. The proximity as well as similar size and east-west rupture extent of the earthquakes enables comparison of the computed tsunami wave fields for distinct, well-constrained faulting mechanisms and assessment of sensitivity to local bathymetric features.

2. Materials and Methods

We seek finite fault models for the 2021 megathrust and 2023 outer rise M_W 7.7 earthquakes southeast of the Loyalty Islands with optimal match to their respective seismic and tsunami records. The iterative refinement procedure begins with a starting model from seismic data inversion that defines the seafloor excitation for modeling of tsunami waves at tide gauge and deep-water stations selected based on data and bathymetry quality. Comparison of computed and recorded signals at the water-level stations guides refinement of pertinent source parameters for another round of finite fault inversion until satisfactory convergence with the tsunami records is achieved.

2.1. Finite Fault Inversion

Finite fault models represent an important tool for describing earthquake kinematics as functions of time and space. The methodology has evolved significantly over the last half-century from simple point source models in homogenous elastic half-space (Madariaga, 2015). The fault surface is subdivided into small segments or subfaults with parameterized source time functions and precomputed Green's functions at sensor locations. When primary source parameters such as the fault geometry, epicenter location, and rupture speed are defined, finite fault inversions of recorded seismic waves can be applied to constrain the time-varying slip on each subfault to characterize the rupture processes (Hartzell & Heaton, 1983; Kikuchi & Kanamori, 1982; Olson & Apsel, 1982).

Finite fault models for the 2021 M_W 7.7 thrust-faulting earthquake have been produced through inversion of seismic waves alone by the USGS-NEIC (https://earthquake.usgs.gov/earthquakes/eventpage/us6000dg77/finite-fault) and by Ye et al. (2021), whereas tsunami-only inversions or forward modeling were performed by Gusman et al. (2022) and Roger et al. (2023). There are differences in these models in whether coseismic slip extended to the upper portion of the megathrust, which can be important for tsunami excitation. We follow Ye et al. (2021) in prescribing a depth-varying dip of the megathrust guided by the Slab2 model (Hayes et al., 2018), and explore the effects of lower rupture velocity and rigidity on the shallow megathrust in matching tsunami waveforms from multiple stations around the source.

A finite fault model for the 2023 M_W 7.7 normal-faulting earthquake was produced by the USGS-NEIC (https://earthquake.usgs.gov/earthquakes/eventpage/us6000kd0n/finite-fault), but the body wave data fitting is very poor for the posted model (as of the writing of this paper), so it is not reliable as an initial approximation for iterative refinement. We obtain a new model for this event by adopting the strike (80°) and rake (−90°) of the USGS-NEIC W-phase solution while perturbing the less well constrained dip over a 35° range to optimize the fit to the recorded seismic and tsunami waveforms.

2.2. Tsunami Modeling

Implementation of a finite fault model with Okada's (1985) elastic half-space solution and Tanioka and Satake's (1996) correction for seafloor slope defines the earth-surface deformation time history for tsunami excitation. NEOWAVE is a well validated code that incorporates nonhydrostatic effects and shock-capturing capabilities in modeling tsunami generation, propagation, and inundation over a system of two-way nested computational grids (Yamazaki et al., 2009, 2011a, 2023). The level-1 grid, as shown in Figure 2a, extends across

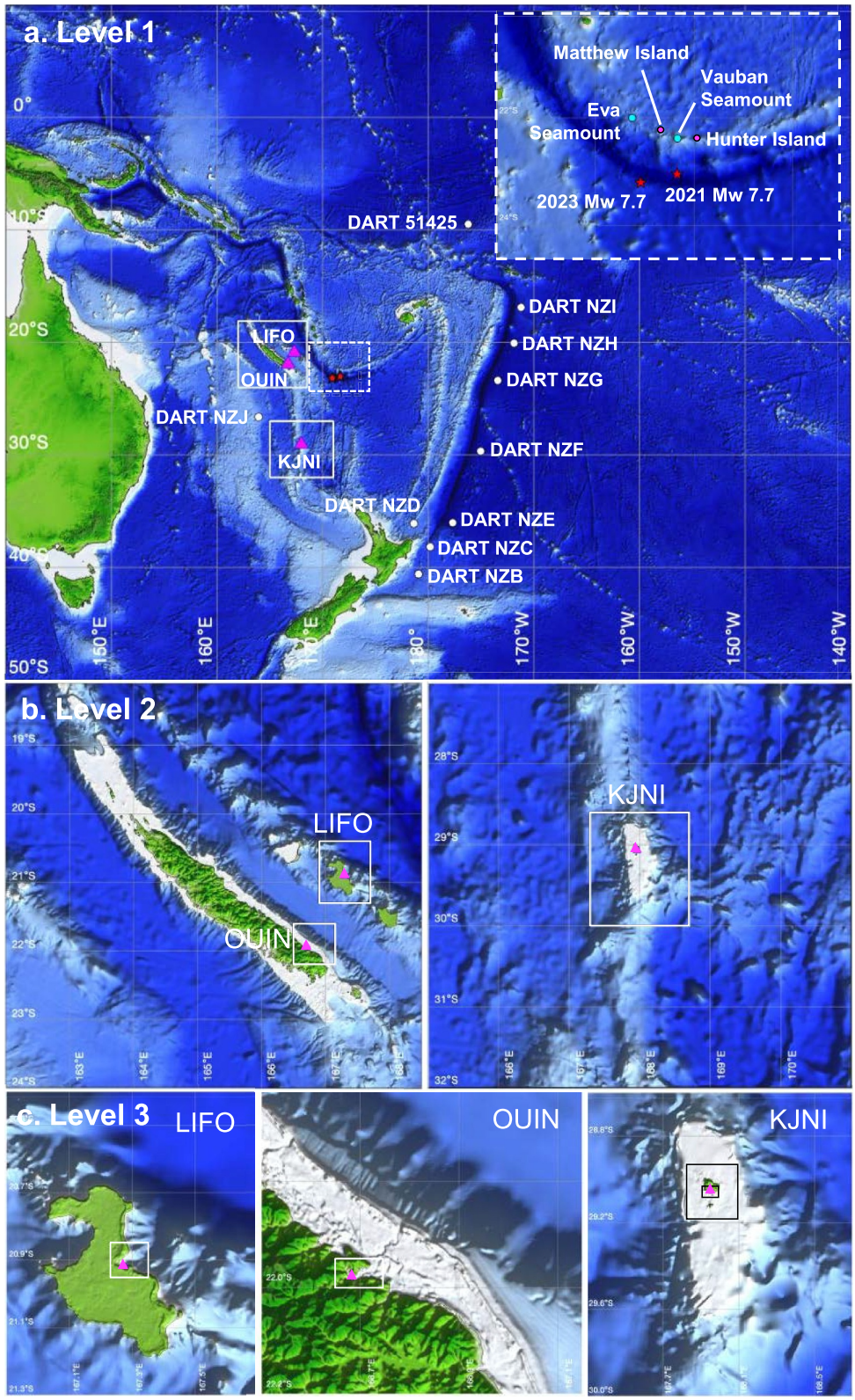

Figure 2. Layout of computational grids and location maps for water-level stations, epicenters, and near-source bathymetric features. (a) Level-1 grid with white solid rectangles delineating level-2 grids and dashed rectangle for the inset map around the tsunami sources. (b) Level-2 grids with layout of level-3 grids. (c) Level-3 grids with layout of level-4 grids at LIFO and QUIN and level-4 and 5 grids at KJNI. White circles and pink triangles indicate DART and tide gauge locations. Base maps generated from GEBCO and TSUCAL and water level station locations from the UNESCO IOC.

the southwest Pacific at 2 arcmin (~3,800 m) resolution for propagation from the source to DART (deep-ocean assessment and reporting of tsunamis) stations with optimal dispersion (Li & Cheung, 2019). Numerous tide gauges across the southwest Pacific recorded the 2021 and 2023 tsunamis (e.g., Roger et al., 2023), but due to availability of quality near-shore bathymetry, only three are considered for high-resolution modeling. The level-2 computation telescopes from 30 arsec (~950 m) to 1 arcsec (~32 m) resolution at the Lifou Island and Ouinne tide gauges and to 0.3 arcsec (~9 m) at the Northfolk Island tide gauge with two and three additional levels of grid nesting, respectively (Figures 2b and 2c). The digital elevation model includes GEBCO14 at 30 arcsec (~950 m) for the southwest Pacific, TSUCAL at 5.76 arcsec (~178 m) and 25 m resolution around Lifou Island and Ouinne (Roger et al., 2021), and gridded data at 1.8 arcsec (~56 m) and 0.36 arcsec (~11 m) for Norfolk Island (Roger, 2022).

DART systems, which have an illustrious history of development and application (Bernard et al., 2023), currently employ a dual-mode sampling rate to monitor ocean conditions and detect tsunamis. Although transmitted data can be time-averaged, the device itself continuously records the sea-surface elevation at 15-s intervals. The standard 15-min transmission mode is intended to monitor the function of the devices and can provide data on tidal fluctuations. A tsunami detection algorithm can place the system under event mode, where data is transmitted at 15 s for 4 min after the triggering event. When this occurs, the data for the hour preceding the event mode and the following 3 hours is re-transmitted at 1 min intervals to resolve the tsunami signals and any precursors. The three tide gauges considered in the present study have a consistent sampling interval of 1 min. The raw signals from DART and coastal gauge stations are contaminated with tidal fluctuations and other long-period oscillations unrelated to tsunami events. The tides were removed using a 7th-order digital Butterworth filter with high-pass and low-pass cutoffs of 2 hr and 4 min, respectively. The filter was applied to each station's 10-hr time series to capture the tidal oscillations for removal, and wave amplitude spectra for each station were computed over 4 hr after tsunami arrival.

3. Preferred Source Models

The finite fault modeling uses global data sets of teleseismic *P* and *SH* waves in least squares kinematic inversions for the 2021 and 2023 M_W 7.7 earthquakes. The water-level records for both events were not available at every station listed in Figure 2a for this study. Some of the DART stations were deployed after the 2021 event. However, the distribution of available data around the source region is sufficient for constraining the rupture mechanism through forward modeling of each tsunami. The iterative refinement procedure leads to the preferred models for the thrust-faulting and normal-faulting earthquakes with distinct source parameters, slip distributions, and seafloor deformation patterns for a comparative study (Table 1, Figure 3).

3.1. The 2021 Thrust-Faulting Event

Tsunami forward modeling for the starting model of Ye et al. (2021) showed systematically lower amplitude and longer period compared to the recorded signals, supporting the likelihood of shallow slip near the trench as indicated by the finite fault models of USGS-NEIC and Gusman et al. (2022). While maintaining the fault surface to approximate Slab2 (Hayes et al., 2018), we altered the shallow source velocity structure and moved the poorly resolved hypocenter up-dip to (23.0634°S, 171.682°E) at a depth of 0.8 km into rock below 6 km of water to increase the short-period oscillations observed in the tsunami records. This shifts the location of peak slip on the fault surface to shallower depth and a suite of inversion models with different source velocities was used to forward-model tsunami signals in matching the records.

The preferred finite-fault model shown in Figure 3a has 277° strike, which is consistent with the northward dipping subduction zone. The 75 × 165 km fault is subdivided into a grid of 10 × 22 subfaults of 7.5 × 7.5 km each extending to the trench. The bathymetry shallows to 1.1 km deep at the northern end of the rupture model. The dip varies from 5° in the shallowest row to 38° in the deepest row. The centroid depth of 12.4 km is considerably smaller than the USGS-NEIC w-phase and GCMT best double-couple solutions (Table 1). Good fits that accounts for 85% of the waveform power are found for the teleseismic *P* and *SH* waves (Figure S1 in Supporting Information S1). The shallower rupture depth results in an increased peak slip to 7.5 m, concentrated at the center of the fault grid. The seismic moment is 4.37×10^{20} Nm (M_W 7.69). The limit for overall rupture velocity across the fault surface is 2.5 km/s for a subfault rise time of 13 s.

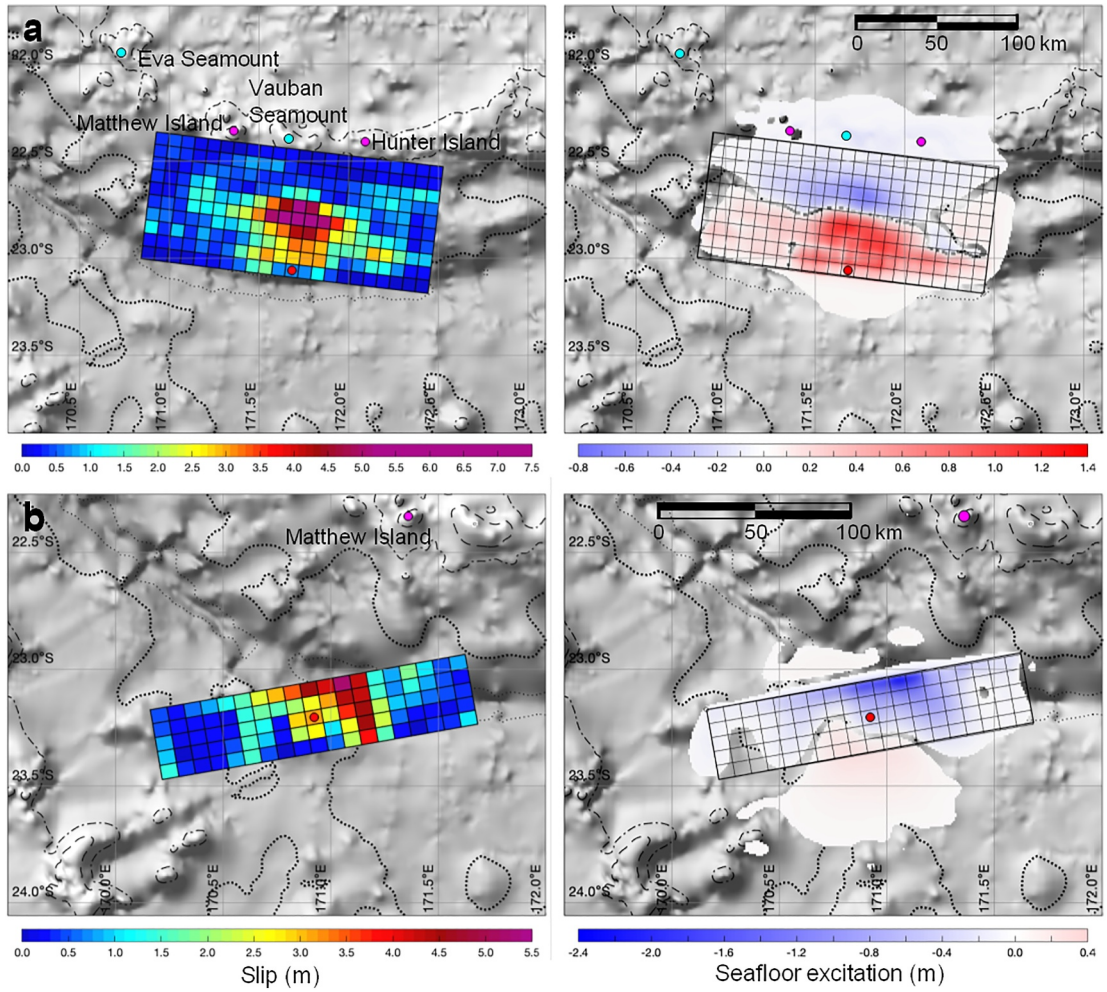

Figure 3. Slip distribution (left column) and seafloor deformation (right column) for preferred source models. (a) The 2021 M_W 7.7 thrust-faulting earthquake. (b) The 2023 M_W 7.7 normal-faulting earthquake. Red circles indicate epicenter locations and cyan and magenta circles identify adjacent seamounts and islands. Isobaths are at 1,000 m (dash), 2,000 m (dot dash), 4,000 m (bold dot), and 6,000 m (fine dot) with base map generated from GEBCO.

The increased tsunami excitation in deeper water through the iterative source refinement leads to improved agreement at the three coastal tide gauges and seven DART stations considered for this event (Figure 4). The tsunami derives most of its energy from the uplift patch adjacent to the trench (Figure 3a). The spectral signals reflect the seafloor deformation pattern and local water depth, but are strongly modulated by resonance oscillations along island chains (Cheung et al., 2013). Greater emphasis is placed on matching the DART observations away from landmasses in selecting the preferred source model. The computed amplitude spectra generally reproduce the observed dominant harmonics of less than ~30 min and align with longer-period peaks augmented by background oscillations. There are notable short-period later arrivals from wave dispersion associated with the near-trench seafloor uplift and detailed features of the deformation pattern as well as wave scattering over seamounts and around small islands. A notable exception is DART 51425, where the observed signal appears to drop in sampling rate from 1 to 15 min at ~4 hr past the USGS-NEIC origin time and that leads to loss of shorter-period waves reducing the quality of the comparison with the model results.

The computed initial arrivals match the observed waveforms reasonably well, including those at the Ouinne (OUIN) and Norfolk Island (KJNI) tide gauges as well as the DART stations to the north and southeast of the tsunami source (See Figure 2a for location). The Lifou (LIFO) tide gauge is located in the Loyalty Islands, where the model overestimates the observed spectral signals between 5 and 10 min that are most sensitive to edge waves over insular shelf and reef complexes (Cheung et al., 2013). With the computed spectral signals in this range

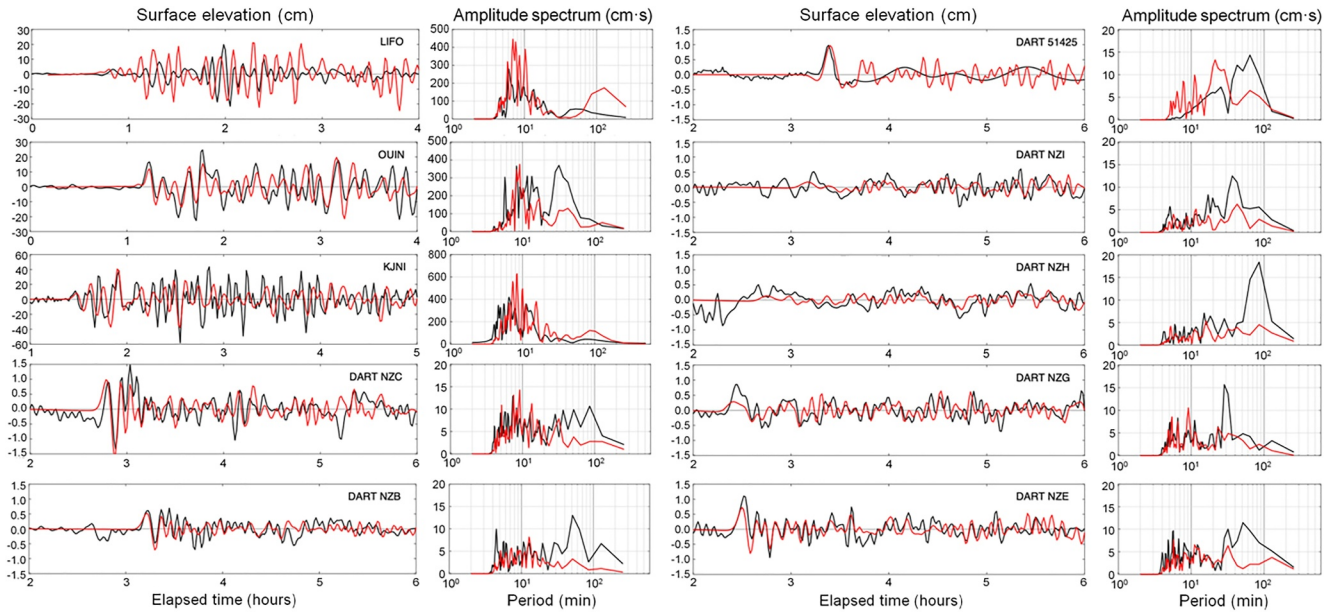

Figure 4. Computed (red) and observed (black) tsunami waveforms and spectra at tide gauge and DART stations for the 2021 M_W 7.7 thrust-faulting earthquake. Vertical axis range remains the same among DART stations, but varies with coastal tide stations for signal presentation.

validated by DART records, the discrepancy is likely due to the insular bathymetry used in the modeling. The DART observations to the east, most notable at NZI and NZH, exhibit relatively strong background oscillations that mask the initial tsunami waves with comparable harmonic components, but the comparison with model results show improved agreement with the shorter-period later arrivals from dispersion. Despite the recorded background noise and model uncertainty, the comparison at multiple stations aids in constraining the source mechanism and also provides validation and assessment of the computed tsunami.

3.2. The 2023 Normal-Faulting Event

The starting finite fault model is based on the USGS-NEIC W-phase geometry (Table 1); the inversion of *P* and *SH* signals led to a rather deep slip distribution for an outer rise slab bending event. We then forward modeled faulting solutions for varying dip and hypocentral depth for the two nodal plane options generated in the inversion. The fault covers a total area of 152 × 40 km and is subdivided into 8 × 8 km subfaults with 19 columns along strike and 5 rows along dip. The preferred finite fault model is based on the southward dipping nodal plane solution with 80° strike and 32.5° dip. The dip for this model, optimized by minimizing residual variance over models with dip increments of 2.5°, is significantly lower than the USGS NEIC W-phase solution of 51° (Table 1). The hypocenter is located 13.6 km into rock under 4 km of water and the centroid depth is 15.8 km. The peak slip is concentrated northeast of the epicenter toward the trench beneath deeper water (Figure 3b). Good matches to the teleseismic body waves that account for 66% of the waveform power are produced by the preferred model (Figure S2 in Supporting Information S1). The seismic moment is 4.23×10^{20} Nm (M_W 7.68). The limit for average rupture velocity across the fault surface is 2.5 km/s for a subfault rise time of 15 s.

The slip distribution computed with the USGS epicenter produces accurate tsunami arrival times at water-level stations to the north and south of the source, but late and early arrivals at stations to the east and west, respectively. Because this systematic timing offset is not observed in the 2021 event with an adjacent source location, it is unlikely the result of bathymetric or computational errors. The epicenter of this event was shifted to (23.206°S, 170.922°E) approximately 20 km eastward, to improve the timing at the eastern and western stations. The computed slip distribution is simply shifted eastward with the new epicenter for tsunami modeling. The initial arrivals are closely aligned with the observations at NZF and NZE east of the source, but are still early at the western stations, most notable LIFO, OUIN, and NZJ (Figure 5). The shifted slip distribution also produces improved agreement in the amplitude and phase of the later arrivals. Additional eastward shift can further improve

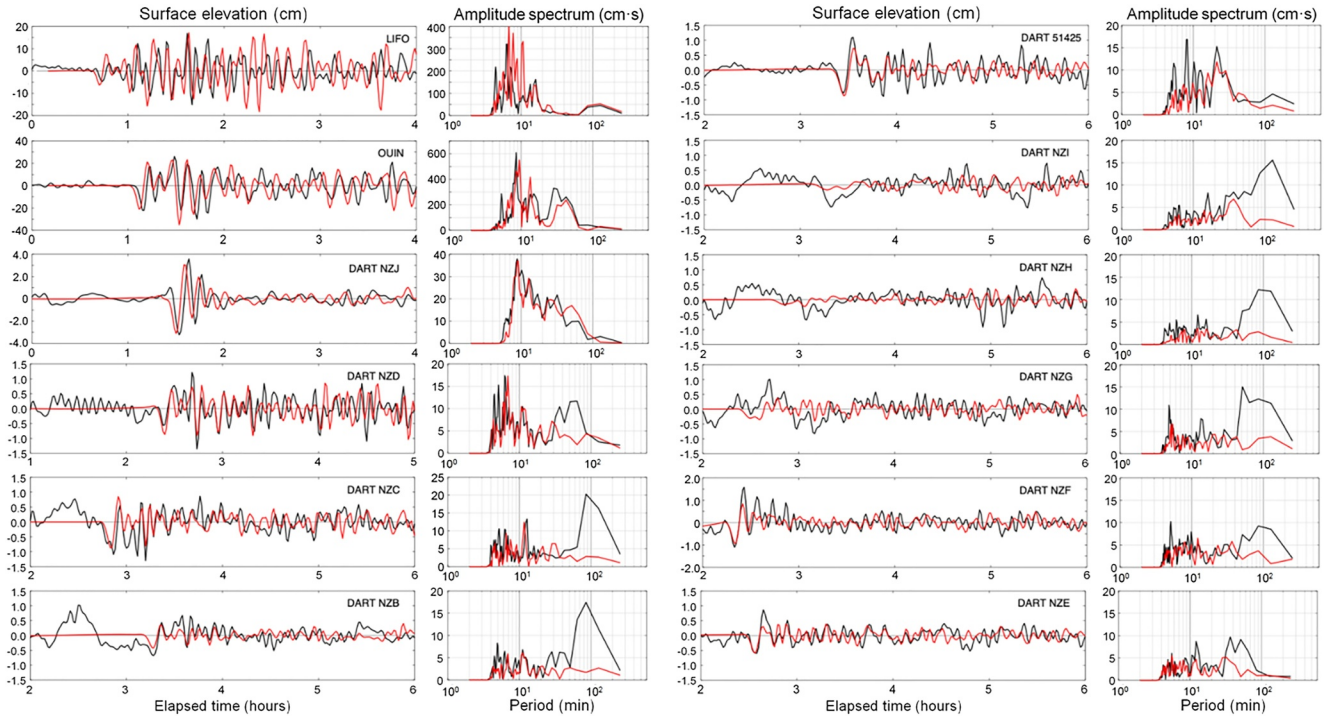

Figure 5. Computed (red) and observed (black) tsunami waveforms and spectra at tide gauge and DART stations for the 2023 M_W 7.7 normal-faulting earthquake. Vertical axis range varies among stations for signal presentation.

the overall agreement in arrival time, but this is not considered given the uncertainty bound for the epicentral location.

The computed waveforms provide a reasonable fit to the observations for several cycles after arrival (Figure 5). This is particularly true for stations 51425, LIFO, OUIN, NZJ, and NZF over a wide azimuth around the source. The overestimation of the 5–10 min signals is also evident at LIFO as in the 2021 event, but with a smaller overall effect to the waveform due to stronger tsunami signals outside this band that are well matched by the model. The DART records to the southeast and northeast of the source exhibit a relatively high level of background noise compared to the tsunami signals (i.e., NZB, NZI, NZH, and NZG). The comparison of the initial arrivals is obscured by the long-period background oscillations, but the observed and computed shorter-period dispersive waves show good amplitude agreement. The large negative arrivals at all stations suggest the tsunami motion is dominated by the narrow strip of subsidence near the trench (Figure 3b), resulting in smaller overall wave periods compared to the 2021 thrust faulting beneath the upper plate slope.

4. Tsunami Generation and Propagation

The calibrated source models for the 2021 megathrust and 2023 outer rise M_W 7.7 earthquakes with similar east-west rupture extents on opposing sides of the Southern Vanuatu Trench provide a robust case study for contrasting tsunami characteristics in relation to the source mechanisms and bathymetric features. The nonhydrostatic modeling with NEOWAVE can resolve tsunami generation from the compact sources, flow over steep volcanic slopes, and dispersion of short-period waves for any subtle variability between the two events. The model results are elaborated in terms of the source-region and near and far-field waveforms as well as the respective radiation patterns across the southwest Pacific.

4.1. Source-Region Waveform

The 2021 thrust-faulting earthquake occurred immediately north of the trench with a total rupture time of 55 s. The shallow slip of 7.5 m has a greater surface expression than the USGS and starting finite fault models. The computed seafloor uplift and subsidence reach 1.31 and 0.78 m (Figure 3a). The excitation from the relatively

compact faulting attenuates over the water column to give sea-surface uplift and drawdown of 0.95 and 0.44 m at the end of the rupture. Figure 6a illustrates the subsequent oscillations near the source. The more energetic sea-surface uplift in deeper water dominates the resulting tsunami as evidenced by the strong leading crest 5 min after the earthquake. The seafloor subsidence on the upper slope produces a weak leading trough to the north. The tsunami has largest amplitude perpendicular to the trench, which is characteristic of an interplate megathrust earthquake with trench-parallel rupture. The initial sea-surface uplift also generates oscillations at the source with a series of attenuating radiated waves. At 10 min, Vauban Seamount appears to refract and focus wave energy to the north. Shallow seamounts and insular shelves are prone to trapping of tsunami waves (Cheung et al., 2013), and gradual release of the trapped energy from Vauban Seamount as short-period radiated waves is evident by 15 min. Although the two systems of radiated waves spread over a 360° azimuth, the energy in east-west directions are refracted northward over the upper plate slope. Additionally, small amplitude, longer-period diffracted waves generated by the leading crests are observed to propagate east and west.

In contrast, the 2023 outer rise earthquake has its source on the south side of the trench, southwest of the nearby Matthew Island (Figure 3b). The preferred finite fault model has a peak slip of 5.2 m and a rupture time of 45 s. The computed seafloor uplift and subsidence reach 0.30 and 2.37 m giving rise to 0.20 m uplift and 0.97 m drawdown of the sea surface at the end of the rupture. This normal-faulting earthquake primarily generates a tsunami through seafloor subsidence with a prominent leading trough (Figure 6b). The amount and area of the initial sea-surface drawdown are comparable to those of the uplift in the 2021 event, suggesting similar energy levels in the two tsunamis. The upswing of the initial drawdown at the source and the subsequent radiated waves are evident in the wave fields at the 5 and 10-min marks. The seafloor uplift produces a weak leading crest to the south. The leading waves are also the strongest perpendicular to the trench due to the rupture alignment. By 15 min, refracted-diffracted waves near Matthew Island are observed with a similar, but weaker pattern on the south side compared to the short-period radiated waves from Vauban Seamount in the 2021 event. Additionally, Eva Seamount appears to focus wave energy through refraction in a way not observed in the 2021 event. These observations highlight the differences in tsunami generation and transformation in relation to source mechanism and local bathymetry (See Movies S1 and S2 for complete sequences of the source-region wave processes for the 2021 and 2023 events).

4.2. Near and Far-Field Waveforms

Tsunami waves are strongly influenced by bathymetric features, with their local speed and direction dependent on water depth and its variation. The effects are most prominent in the near field along the curved plate boundary (Figure 7). The epicenter of the 2021 thrust-faulting earthquake is immediately south of Vauban Seamount, which focuses the leading wave to the north. At 30 min after the earthquake, radiation of the energy trapped over Vauban Seamount can be seen traversing east and west along Hunter Ridge on the north side of the trench. Refraction and diffraction of the leading wave around Matthew Island also focuses energy to the north. In comparison, the tsunami waves generated by the 2023 event refract and diffract around Matthew Island to a lesser extent due to the location of the deformation patch far to the southwest on the outer rise (Figure 3b). However, the source location provides a direct approach to Eva Seamount where significant wave amplification is observed. At the 30 min mark, refraction of the tsunami around Eva Seamount and Matthew Island amplifies the leading waves toward the north-northwest and north-northeast in alignment of the source with the two bathymetric features. In contrast to radiation, the diffracted waves from Matthew Island attenuate azimuthally from the north side to the east and west with weaker presence along Hunter Ridge.

At 40 min, the waves from the 2021 and 2023 tsunamis exhibit different characteristics in the area between Vanuatu and the trench. The northwest traveling waves generated by the 2021 event show coherent crests and troughs spanning the upper plate slope. This is due to refraction of radiated waves from Vauban Seamount as they approach Vanuatu, increasing the wave amplitude to the southern and western parts of the islands. The 2023 tsunami does not extend west of 170°E with the same level of energy due to azimuthal attenuation of diffracted waves around Matthew Islands. By 50 min, the tsunami pattern shows similarities between the two events despite the reversed polarity of the leading wave. Both tsunamis appear to diffract through the passage between Aneityum and Tanna, while the 2021 tsunami exhibits more concentrated wave energy wrapping around Vanuatu from the south and west (See Figure 1 for location map). Due to the location and strike of both ruptures, neither event presented a direct tsunami threat to the main island of New Caledonia. The Isle of Pines immediately to the southeast is in the path of tsunami waves from the source and its extensive shallow lagoon and reef systems may

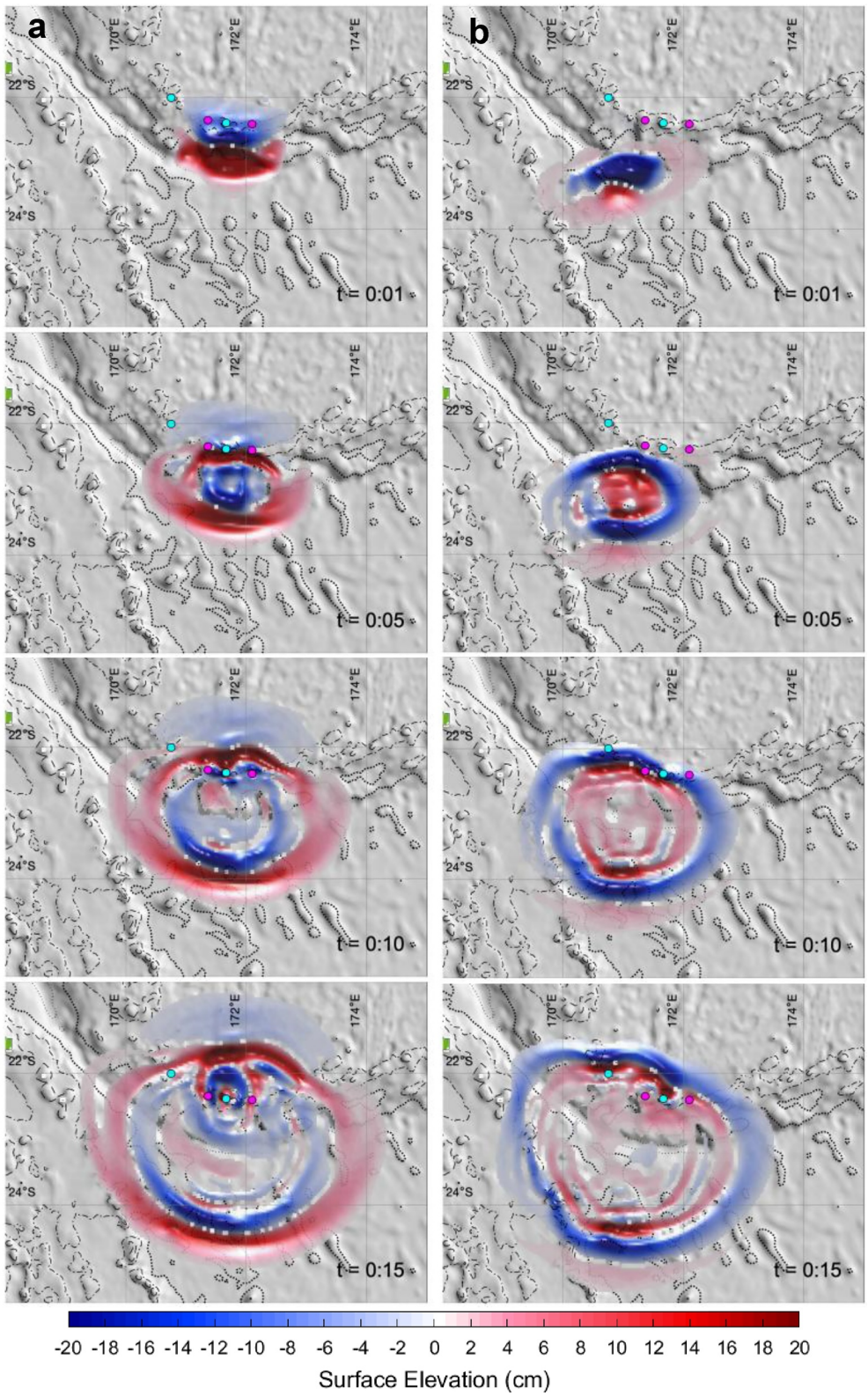

Figure 6. Computed initial tsunami waves at 1, 5, 10, and 15 min after their respective origin times. (a) The 2021 M_W 7.7 thrust-faulting earthquake. (b) The 2023 M_W 7.7 normal-faulting earthquake. Cyan circles indicate Eva Seamount (left) and Vauban Seamount (right) and magenta circles indicate Matthew Island (left) and Hunter Island (right) with significant influence to the tsunamis. Isobaths are at 1,000 m (dash), 2,000 m (dot dash), 4,000 m (bold dot), and 6,000 m (fine dot) with base map generated from GEBCO and time t in hr:min.

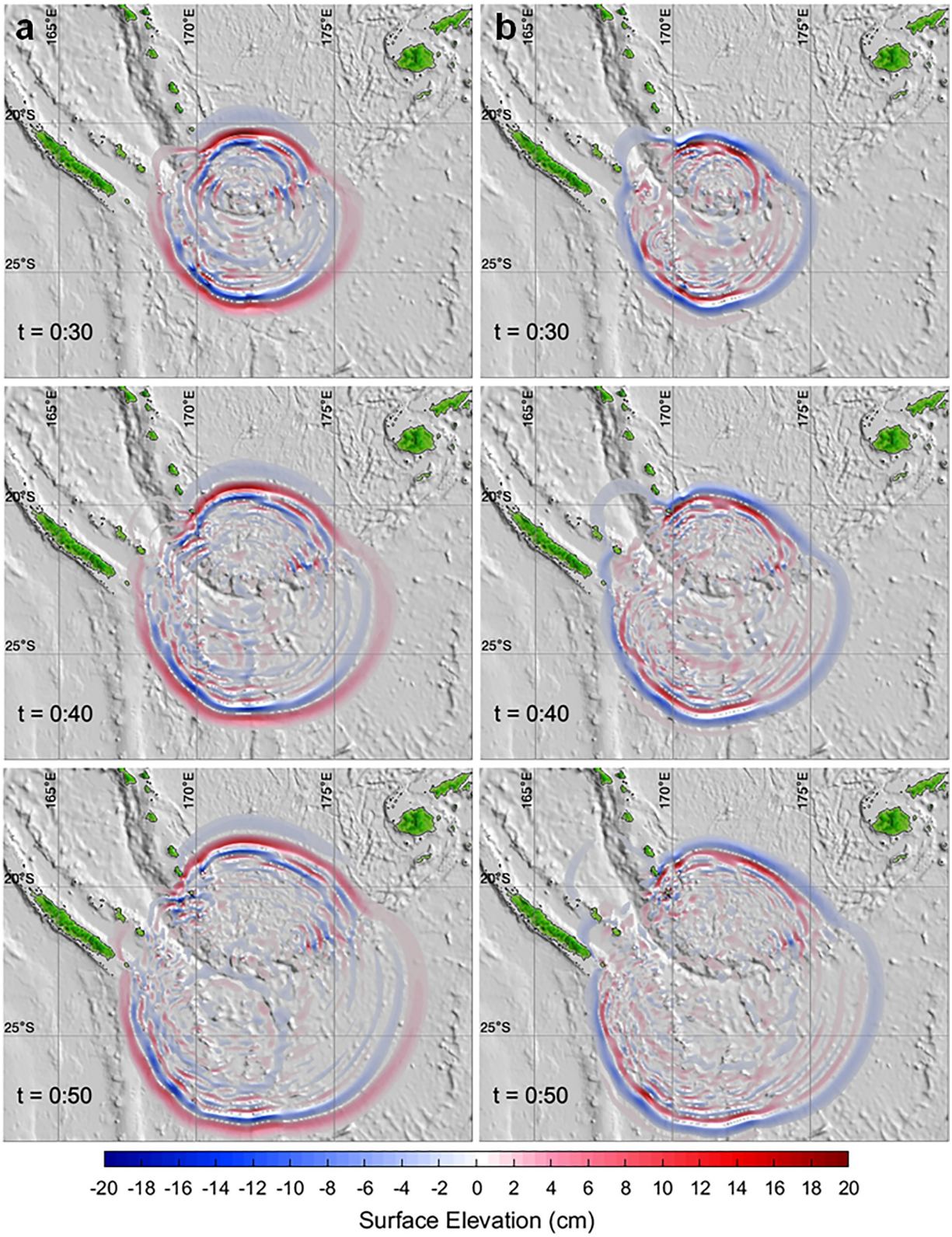

Figure 7. Computed near-field tsunamis at 30, 40, and 50 min after their respective origin times. (a) The 2021 M_W 7.7 thrust-faulting earthquake. (b) The 2023 M_W 7.7 normal-faulting earthquake. Base map generated from GEBCO and time t in hr:min.

amplify short period dispersive waves to produce large runup (e.g., Roeber et al., 2010). Apart from the reversed polarity, the two tsunamis south of the trench are very similar due to the absence of bathymetric features immediately south of the sources.

The leading wave amplitude tends to even out in the along-crest directions as tsunamis propagate into the far field, except for local amplification over seamounts and around islands. The overall wave patterns for both events are similar albeit with opposing phase and different amplitude (Figure 8). Long-crested waves are preserved in three primary directions related to the water passages between Australia, New Zealand, Fiji, and Vanuatu/New Caledonia. Islands and submarine ridges or any abrupt oceanic slope transitions trap progressive waves in the form of local oscillations (Bai et al., 2022; Cheung et al., 2013). Superposition of subsequent radiated energy in opposing directions creates elaborate standing waves crisscrossing the ocean among bathymetric features (Bai et al., 2015). The short crested waves observed at the 2 and 3-hr marks within the North and South Fiji Basins suggest development of resonant oscillations. This explains the persistent short-period signals recorded at the tide gauges and DART stations in both events (See Movies S3 and S4 for complete sequences of the near and far-field wave propagation for the 2021 and 2023 events).

4.3. Maximum Surface Elevation

The maximum surface elevation plots in Figure 9 reveal distinct propagation patterns of the tsunamis generated by the 2021 thrust-faulting and 2023 normal-faulting earthquakes. The 2021 tsunami in the near field is typical of a megathrust event with the main lobe normal to the trench and higher amplitude northward due to shoaling over the upper plate slope. The main lobe is also amplified and focused by Vauban Seamount located immediately north of the main deformation patch (Figure 6a). There is a pair of rapidly attenuating sidelobes from refraction of radiated waves over the upper-plate slope on either side of the main lobe. The 2023 tsunami has a leading trough generated by seafloor subsidence followed by a prominent wave crest from rebound of the initial drawdown at the source. The maximum crest amplitude has a main lobe along the trench-normal to the south, but the corresponding lobe to the north is much weaker. The more prominent lobes in the north-northeast and north-northwest are due to wave refraction around Matthew Island and Eva Seamount (Figure 6b). The directionality follows the orientation of the tsunami source and the respective bathymetric features.

The 2023 tsunami has comparable crest amplitude and overall energy to the 2021 event, but narrower lobes from the upswing around the peak of the initial sea-surface drawdown, where nonhydrostatic effects associated with the vertical flow momentum are more prominent. The leading crest is generally continuous for both tsunamis (Figures 7 and 8), but refraction over seamounts creates localized concentrations of energy in the general propagation direction. The elevation plots show the directionality and energy of the largest crest that might shift from the leading to trailing waves as the tsunami propagates away from the source (Figures 4 and 5). This is particularly the case outside the North and South Fiji Basins as the leading wave attenuates due to azimuthal spreading. Constructive inference of shorter period waves generated by scattering around submarine ridges and seamounts behind the leading wave gives the more elaborate energy distribution in the far field.

With a large leading trough in the 2023 tsunami, the maximum absolute value of the sea surface elevation provides a more complete description of the propagation patterns for comparison of the two events (Figure 10). The directionality of each event remains similar when wave troughs are included in describing the propagation pattern. The large leading trough of the 2023 tsunami results in wider energy lobes and reveals a sidelobe toward the Loyalty Islands that is absence in the maximum surface elevation plot (Figure 9). This is because the shorter period crest from upswing of the initial drawdown is refracted more effectively to the north by the upper plate slope, thereby reducing the energy in the along-strike directions. The energy distribution appears more concentrated around the source, with larger amplitude waves not observed traveling as far north or south compared to the 2021 event. This is likely due to more rapid attenuation of the shorter period waves generated in deeper water by a narrower deformation patch in the outer rise near the trench. The longer-period 2021 tsunami waves generated over the upper plate slope result in less dispersion and higher amplitude reaching farther from the source region. The two events have slightly different directionality associated with the fault orientation at the source. The similarity of the tsunamis to the south attests to the absence of major bathymetric features near the source that might redirect the energy through refraction.

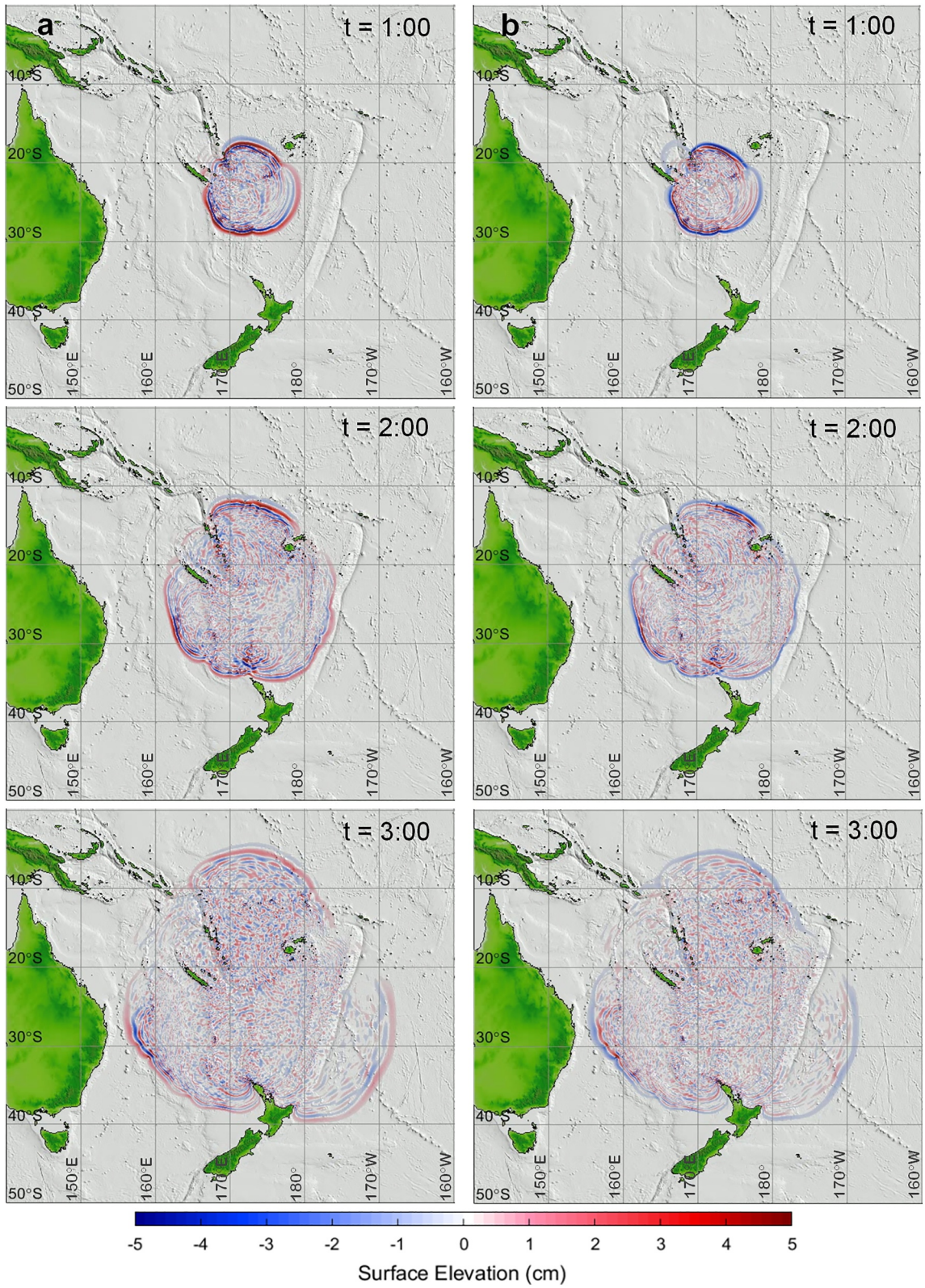

Figure 8. Computed far-field tsunamis at 1 hr, 2 hr, and 3 hr marks after their respective origin times. (a) The 2021 M_W 7.7 thrust-faulting earthquake. (b) The 2023 M_W 7.7 normal-faulting earthquake. Base map generated from GEBCO and time t in hr:min.

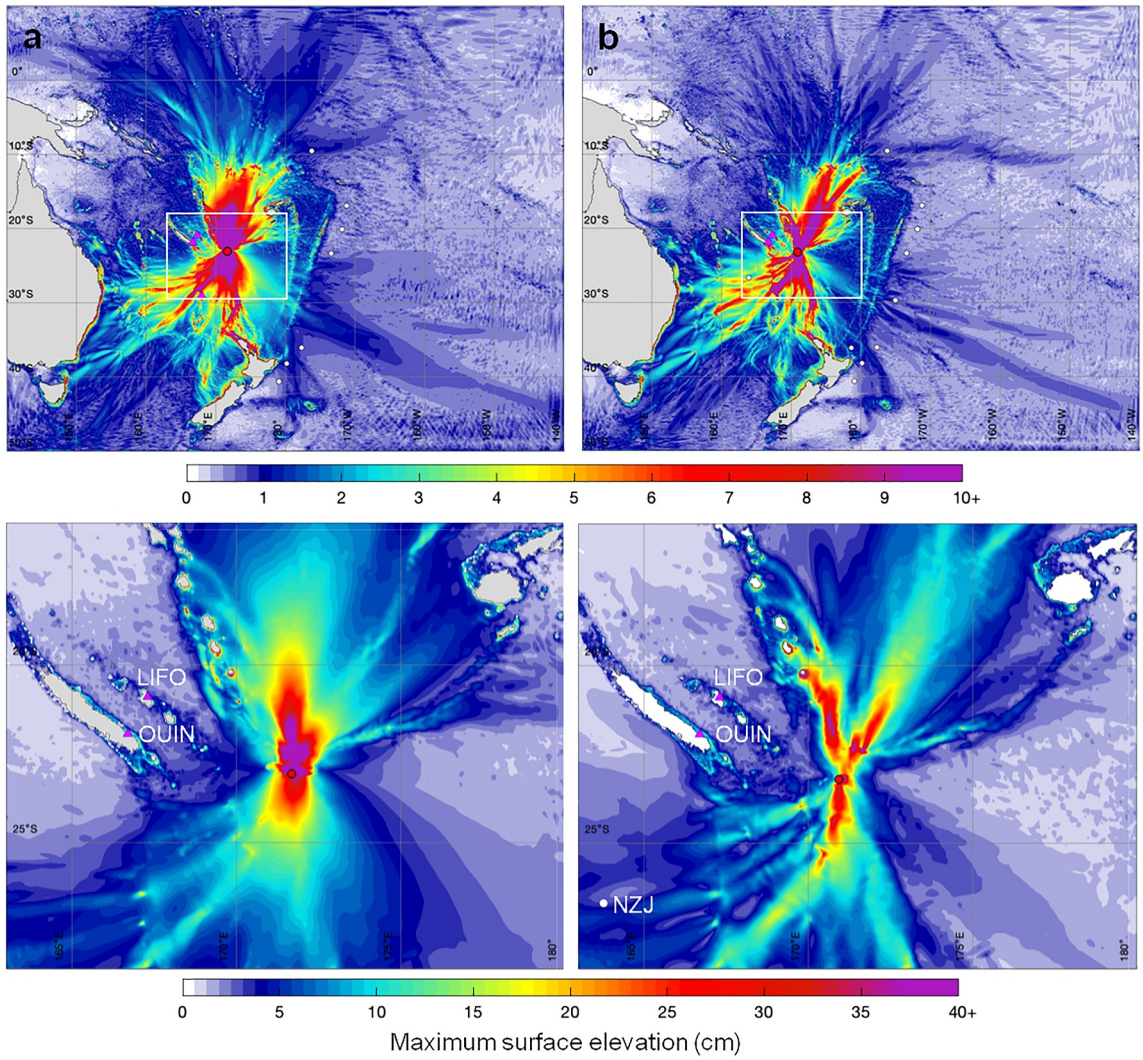

Figure 9. Maximum crest amplitude in the near and far fields. (a) The 2021 M_W 7.7 thrust-faulting earthquake. (b) The 2023 M_W 7.7 normal-faulting earthquake. White rectangles in the upper panels delineate the near-field region shown in the lower panels with base maps generated from GEBCO. Red circles indicate the earthquake epicenter locations. Magenta triangles and white circles indicate locations of tide gauge and DART stations.

5. Discussion and Conclusions

The iterative refinement procedure with nonhydrostatic modeling of dispersive tsunami waves is effective in constraining rupture parameters over the relatively compact sources of the 2021 and 2023 M_W 7.7 earthquakes southeast of the Loyalty Islands. Although the 2021 thrust-faulting geometry is consistent with the northward dipping subduction zone, the normal-faulting geometry of the 2023 event is not as clear tectonically. The aftershock sequence involves a wide swath along the outer rise, and the USGS-NEIC finite-fault model reasonably adopts a nearly trench-parallel strike. This is probably not correct as indicated by the poor fits to teleseismic data and the USGS-NEIC W-phase moment tensor. The geometry in our preferred model, which fits the teleseismic and tsunami data very well, is somewhat oblique to the trench (Figure 3b) and has some uncertainty in absolute location as suggested by the slight mismatch of tsunami arrivals, but is similar to minor lineations apparent in the bathymetry. It may be that bending forces reactivate prior structures not exactly aligned with the trench.

The 2021 and 2023 tsunamis have a large leading crest and a large leading trough characteristic of the respective thrust and normal faulting. Vertical seafloor displacements, either in the positive or negative direction, are what primarily set tsunami waves in motion. The tsunami hazard associated with the two source mechanisms cannot be

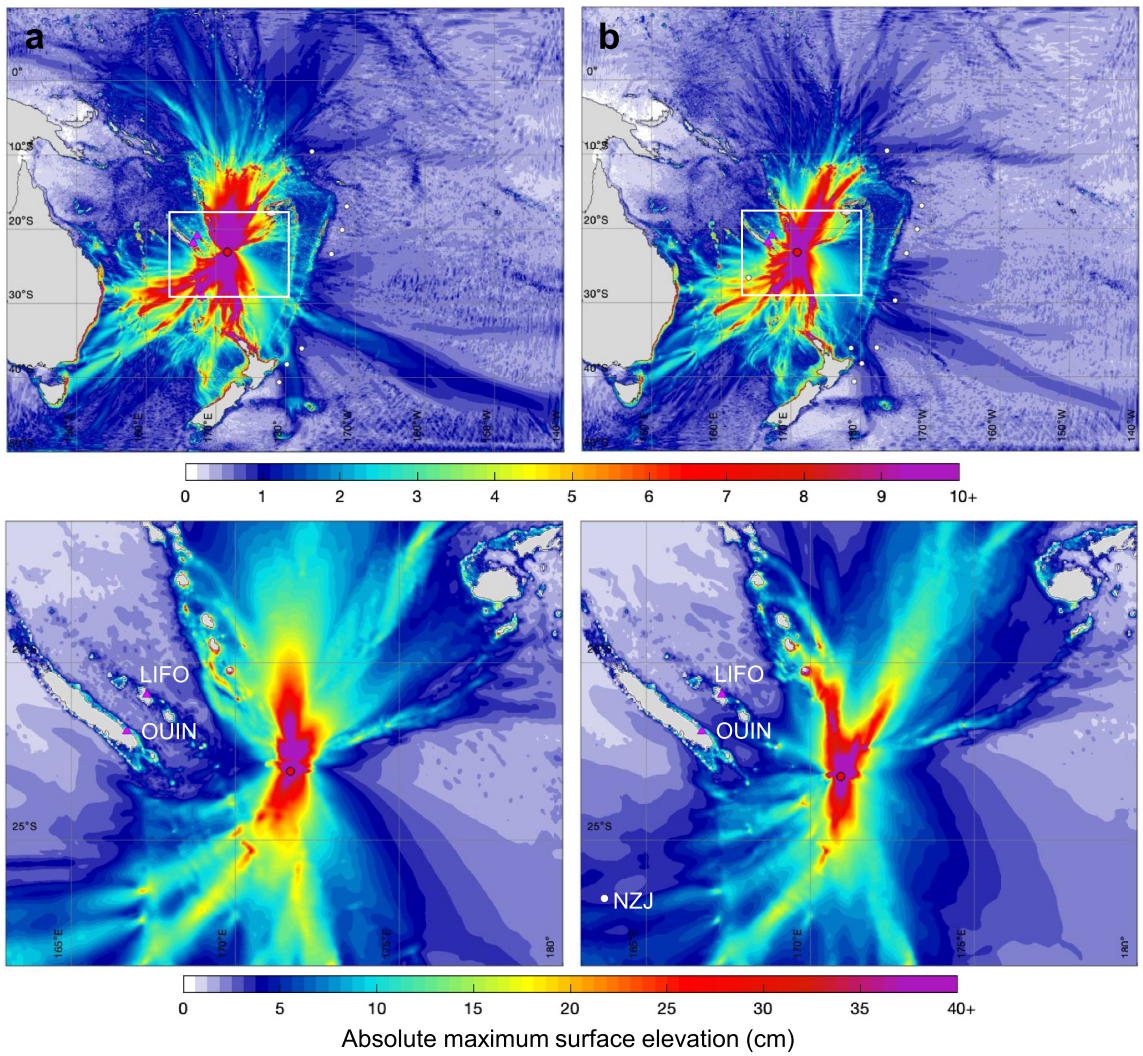

Figure 10. Maximum crest/trough amplitude in the near and far fields. (a) The 2021 M_W 7.7 thrust-faulting earthquake. (b) The 2023 M_W 7.7 normal-faulting earthquake. White rectangles in the upper panels delineate the near-field region shown in the lower panels with base maps generated from GEBCO. Red circles indicate the earthquake epicenter locations. Magenta triangles and white circles indicate locations of tide gauge and DART stations.

fully addressed without runup and inundation calculations. However, several factors on wave dynamics can be considered. A large leading crest generated by seafloor uplift does not necessarily give rise to the most severe coastal impact. Energy tends to accumulate over insular and continental shelves as edge waves, which can generate extensive runup and inundation from constructive interference well after the first arrival (Roeber et al., 2010; Yamazaki & Cheung, 2011). Leading troughs, which characteristically induce a temporary retreat of coastal water, can expose substantial areas of the seafloor and result in turbulent bore formation further offshore. On steep coastal slopes, the upswing of the drawdown from a trough might amplify the impact of the following crest in a local resonance process (Bai, Yamazaki, & Cheung, 2023).

The location of seafloor deformation with respect to surrounding bathymetric features strongly influences the near-field tsunami wave propagation and far-field tsunami energy distribution. Although the east-west trending ruptures of both events result in primary wave directions to the north and south, the southern lobes of both tsunamis are very similar due to absence of large seafloor features immediately south of the sources. However, the earthquake location with respect to the archipelago along Hunter Ridge significantly affects the directionality of tsunami waves northward. The 2021 deformation patch located immediately south of Vauban Seamount produces a prominent energy lobe to the north. Eva Seamount and Matthew Island to the northwest and northeast of the

2023 deformation patch lead to refraction and focusing of the tsunami energy in the respective directions. This highlights the importance of the precise placement of slip in regional tsunami hazard assessment and the complementary advantages in joint seismic and tsunami analysis of earthquake sources.

Despite the differences in the near-field energy distribution and leading wave polarity, the far-field pattern remains consistent between the 2021 and 2023 tsunamis. This similarity is attributed to the many seamounts and small islands, which act as waveguides across the North Fiji Basin, but the wave period also plays a role in the far-field wave amplitude. The width of seafloor deformation and the local water depth have strong influence on the period of the resulting tsunami waves. The 2023 outer rise earthquake, characterized by narrower seafloor deformation in deeper water compared to the 2021 megathrust event, resulted in shorter-period waves typical of normal-faulting events (Baba et al., 2021). This leads to more intricate and narrower energy lobes as shorter-period waves shoal and refract more effectively around seamounts and small islands. Despite being generated by larger seafloor displacement, the waves have comparable initial amplitude and attenuate more rapidly from the source due to nonhydrostatic effects. In contrast, the 2021 thrust-faulting earthquake, with more extensive and uniform seafloor deformation on the upper plate under shallower water, produced longer-period waves that better maintain their amplitude in the far field.

Larger earthquake events located further north along the trench between Vanuatu and New Caledonia, such as the 1875 M_W 8.1–8.2 (Ioualalen et al., 2017) and 1950 M_W 7.9 earthquakes, pose a more direct tsunami risk to local communities. Tsunamis similar to those generated by the 2021 and 2023 M_W 7.7 earthquakes present minimal threat to the main island of New Caledonia but can potentially impact Vanuatu and land masses in the path of the main lobes to the north and south (e.g., Gusman et al., 2022; Roger et al., 2023). Increasing seismic and tsunami monitoring near populated areas is essential. Global seismic network stations are rather sparsely distributed in the southwest Pacific, but are supplemented by more than 50 stations of the Oceania Regional Seismic Network (ORSNET) owned by South Pacific countries, although maintenance in the harsh tropical environment with many cyclones is proving challenging (UNESCO-IOC, 2025). The New Zealand DART network deployed in 2021 has two units in this region and there is a proposed SMART (Science Monitoring and Reliable Telecommunications) subsea cable system between Vanuatu and New Caledonia (Howe et al., 2022). Paleo-tsunami studies can help identify past major events well beyond the last 100 years, providing valuable insights into future risks (Paris et al., 2023). Modeling seismic events, including normal-faulting earthquakes, further north will help determine hazard levels closer to population centers. Implementing these measures will improve preparedness and reduce the risk to vulnerable populations in the region.

Data Availability Statement

Tide gauge and DART station observations were accessed through the IOC water level monitoring website (https://www.ioc-sealevelmonitoring.org/). DEM resources include GEBCO (https://www.gebco.net/data_and_products/gridded_bathymetry_data/), the TSUCAL project (Roger et al., 2021), and high-resolution bathymetry and topography of Norfolk Island (https://geodata.nz/geonetwork/srv/api/records/cc0ed7e4-628b-4445-89b5-4bebbe67fcd2). The finite faults models for the 2021 and 2023 M_W 7.7 earthquakes are provided as Data Sets S1 and S2 in Supporting Information S1.

Acknowledgments
The Gordon and Betty Moore Foundation funded this study through Grant GBMF10787 to the University of Hawaii. T. Lay was supported by the National Science Foundation under Grant EAR-1802364. We thank Jean Roger for providing high-resolution digital elevation models for the southwest Pacific and the two anonymous reviewers along with Bruce Howe for their comments and suggestions on this paper. SOEST Contribution No. 11902.

References

Agranier, A., Patriat, M., Mortimer, N., Collot, J., Etienne, S., Durance, P., & Gans, P. (2023). Oligo-Miocene subduction-related volcanism of the loyalty and three kings ridges, SW Pacific: A precursor to the Tonga-Kermadec arc. *Lithos*, *436*, 106981. https://doi.org/10.1016/j.lithos.2022.106981

Baba, T., Chikasada, N., Imai, K., Tanioka, Y., & Kodaira, S. (2021). Frequency dispersion amplifies tsunamis caused by outer-rise normal faults. *Scientific Reports*, *11*(1), 20064. https://doi.org/10.1038/s41598-021-99536-x

Bai, Y., Liu, C., Lay, T., Cheung, K. F., & Yamazaki, Y. (2023). Fast and slow intraplate ruptures during the 19 October 2020 magnitude 7.6 Shumagin earthquake. *Nature Communications*, *14*(1), 2015. https://doi.org/10.1038/s41467-023-37731-2

Bai, Y., Liu, C., Lay, T., Cheung, K. F., & Ye, L. (2022). Optimizing a model of coseismic rupture for the 22 July 2020 M_W 7.8 Simeonof earthquake by exploiting acute sensitivity of tsunami excitation across the shelf break. *Journal of Geophysical Research: Solid Earth*, *127*(7), e2022JB024484. https://doi.org/10.1029/2022JB024484

Bai, Y., Yamazaki, Y., & Cheung, K. F. (2015). Interconnection of multi-scale standing waves across the Pacific Basin from the 2011 Tohoku Tsunami. *Ocean Modelling*, *92*, 183–197. https://doi.org/10.1016/j.ocemod.2015.06.007

Bai, Y., Yamazaki, Y., & Cheung, K. F. (2023). Intercomparison of hydrostatic and nonhydrostatic modeling for tsunami inundation mapping. *Physics of Fluids*, *35*(7), 077111. https://doi.org/10.1063/5.0152104

Bergeot, N., Bouin, M. N., Diament, M., Pelletier, B., Régnier, M., Calmant, S., & Ballu, V. (2009). Horizontal and vertical interseismic velocity fields in the Vanuatu subduction zone from GPS measurements: Evidence for a central Vanuatu locked zone. *Journal of Geophysical Research*, *114*(B6), 2007JB005249. https://doi.org/10.1029/2007JB005249

Bernard, E., Meinig, C., Titov, V. V., & Wei, Y. (2023). 50 years of PMEL tsunami research and development. *Oceanography*, *36*(2–3), 175–198. https://doi.org/10.5670/oceanog.2023.208

Calmant, S., Pelletier, B., Lebellegard, P., Bevis, M., Taylor, F. W., & Phillips, D. A. (2003). New insights on the tectonics along the New Hebrides subduction zone based on GPS results. *Journal of Geophysical Research*, *108*(B6), 2001JB000644. https://doi.org/10.1029/2001JB000644

Carney, J. N., & Macfarlane, A. (1982). Geological evidence bearing on the Miocene to recent structural evolution of the New Hebrides arc. *Tectonophysics*, *87*(1–4), 147–175. https://doi.org/10.1016/0040-1951(82)90225-6

Cheung, K. F., Bai, Y., & Yamazaki, Y. (2013). Surges around the Hawaiian Islands from the 2011 Tohoku Tsunami. *Journal of Geophysical Research: Oceans*, *118*(10), 5703–5719. https://doi.org/10.1002/jgrc.20413

Cleveland, K. M., Ammon, C. J., & Lay, T. (2014). Large earthquake processes in the Northern Vanuatu subduction zone. *Journal of Geophysical Research: Solid Earth*, *119*(12), 8866–8883. https://doi.org/10.1002/2014JB011289

Gans, P. B., Mortimer, N., Patriat, M., Turnbull, R. E., Crundwell, M. P., Agranier, A., et al. (2023). Detailed $^{40}Ar/^{39}Ar$ geochronology of the loyalty and three Kings Ridges clarifies the extent and sequential development of Eocene to Miocene Southwest Pacific remnant volcanic arcs. *Geochemistry, Geophysics, Geosystems*, *24*(2), e2022GC010670. https://doi.org/10.1029/2022GC010670

Gusman, A. R., Murotani, S., Satake, K., Heidarzadeh, M., Gunawan, E., Watada, S., & Schurr, B. (2015). Fault slip distribution of the 2014 Iquique, Chile, earthquake estimated from ocean-wide tsunami waveforms and GPS data. *Geophysical Research Letters*, *42*(4), 1053–1060. https://doi.org/10.1002/2014GL062604

Gusman, A. R., Roger, J., Power, W., Fry, B., & Kaneko, Y. (2022). The 2021 Loyalty Islands earthquake (M_W 7.7): Tsunami waveform inversion and implications for tsunami forecasting for New Zealand. *Earth and Space Science*, *9*(11), e2022EA002346. https://doi.org/10.1029/2022EA002346

Hartzell, S. H., & Heaton, T. H. (1983). Inversion of strong ground motion and teleseismic waveform data for the fault rupture history of the 1979 Imperial Valley, California, earthquake. *Bulletin of the Seismological Society of America*, *73*(6A), 1553–1583. https://doi.org/10.1785/BSSA07306A1553

Hayes, G., Moore, G. L., Portner, D. E., Hearne, M., Flamme, H., Furtney, M., & Smoczyk, G. M. (2018). Slab2—A comprehensive subduction zone geometry model [Dataset]. *U.S. Geological Survey*, *362*(6410), 58–61. https://doi.org/10.5066/F7PV6JNV

Heidarzadeh, M., Harada, T., Satake, K., Ishibe, T., & Gusman, A. R. (2016). Comparative study of two tsunamigenic earthquakes in the Solomon Islands: 2015 M_W 7.0 normal-fault and 2013 Santa Cruz M_W 8.0 megathrust earthquakes. *Geophysical Research Letters*, *43*(9), 4340–4349. https://doi.org/10.1002/2016GL068601

Howe, B. M., Angove, M., Aucan, J., Barnes, C. R., Barros, J. S., Bayliff, N., et al. (2022). SMART subsea cables for observing the earth and ocean, mitigating environmental hazards, and supporting the blue economy. *Frontiers in Earth Science*, *9*, 775544. https://doi.org/10.3389/feart.2021.775544

Ioualalen, M., Pelletier, B., & Solis Gordillo, G. (2017). Investigating the March 28th 1875 and the September 20th 1920 earthquakes/tsunamis of the southern Vanuatu arc, offshore Loyalty Islands, New Caledonia. *Tectonophysics*, *709*, 20–38. https://doi.org/10.1016/j.tecto.2017.05.006

Kikuchi, M., & Kanamori, H. (1982). Inversion of complex body waves. *Bulletin of the Seismological Society of America*, *72*(2), 491–506. https://doi.org/10.1785/BSSA0720020491

Lay, T., Ye, L., Kanamori, H., Yamazaki, Y., Cheung, K. F., & Ammon, C. J. (2013). The February 6, 2013 M_W 8.0 Santa Cruz islands earthquake and tsunami. *Tectonophysics*, *608*, 1109–1121. https://doi.org/10.1016/j.tecto.2013.07.001

Li, L., & Cheung, K. F. (2019). Numerical dispersion in non-hydrostatic modeling of long-wave propagation. *Ocean Modelling*, *138*, 68–87. https://doi.org/10.1016/j.ocemod.2019.05.002

Li, L., Lay, T., Cheung, K. F., & Ye, L. (2016). Joint modeling of teleseismic and tsunami wave observations to constrain the 16 September 2015 Illapel, Chile, M_W 8.3 earthquake rupture process. *Geophysical Research Letters*, *43*(9), 4303–4312. https://doi.org/10.1002/2016GL068674

Madariaga, R. (2015). Seismic source theory. In *Treatise on geophysics* (pp. 51–71). Elsevier. https://doi.org/10.1016/B978-0-444-53802-4.00070-1

Okada, Y. (1985). Surface deformation due to shear and tensile faults in a half-space. *Bulletin of the Seismological Society of America*, *75*(5), 1135–1154. https://doi.org/10.1785/BSSA0750041135

Olson, A. H., & Apsel, R. J. (1982). Finite faults and inverse theory with applications to the 1979 Imperial Valley earthquake. *Bulletin of the Seismological Society of America*, *72*(6A), 1969–2001. https://doi.org/10.1785/BSSA07206A1969

Paris, R., Pelletier, B., Roger, J., Wassmer, P., & Sabatier, P. (2023). Sedimentary evidence of tsunamis in New Caledonia, southwest Pacific. *Marine Geology*, *463*, 107116. https://doi.org/10.1016/j.margeo.2023.107116

Patriat, M., Collot, J., Danyushevsky, L., Fabre, M., Meffre, S., Falloon, T., et al. (2015). Propagation of back-arc extension into the arc lithosphere in the Southern New Hebrides volcanic arc. *Geochemistry, Geophysics, Geosystems*, *16*(9), 3142–3315. https://doi.org/10.1002/2015GC005717

Patriat, M., Falloon, T., Danyushevsky, L., Collot, J., Jean, M. M., Hoernle, K., et al. (2019). Subduction initiation terranes exposed at the front of a 2 Ma volcanically-active subduction zone. *Earth and Planetary Science Letters*, *508*, 30–40. https://doi.org/10.1016/j.epsl.2018.12.011

Petterson, M. G., Babbs, T., Neal, C. R., Mahoney, J. J., Saunders, A. D., Duncan, R. A., et al. (1999). Geological–tectonic framework of Solomon Islands, SW Pacific: Crustal accretion and growth within an intra-oceanic setting. *Tectonophysics*, *301*(1–2), 35–60. https://doi.org/10.1016/s0040-1951(98)00214-5

Power, W., Wallace, L., Wang, X., & Reyners, M. (2011). Tsunami hazard posed to New Zealand by the Kermadec and Southern New Hebrides Subduction margins: An assessment based on plate boundary kinematics, interseismic coupling, and historical seismicity. *Pure and Applied Geophysics*, *169*(1–2), 1–36. https://doi.org/10.1007/s00024-011-0299-x

Roeber, V., Yamazaki, Y., & Cheung, K. F. (2010). Resonance and impact of the 2009 Samoa tsunami around Tutuila, American Samoa. *Geophysical Research Letters*, *37*(21), L21604. https://doi.org/10.1029/2010GL044419

Roger, J. (2022). Digital elevation model of Norfolk Island and Sydney Bay, Australia [Dataset]. https://geodata.nz/geonetwork/srv/api/records/cc0ed7e4-628b-4445-89b5-4bebbe67fcd2

Roger, J., & Pelletier, B. (2024). A brief history of tsunamis in the Vanuatu Arc. *Natural Hazards and Earth System Sciences*, *24*(10), 3461–3478. https://doi.org/10.5194/nhess-2023-198

Roger, J., Pelletier, B., Duphil, M., Lefèvre, J., Aucan, J., Lebellegard, P., et al. (2021). The M_W 7.5 Tadine (Maré, Loyalty Islands) earthquake and related tsunami of 5 December 2018: Seismotectonic context and numerical modeling. *Natural Hazards and Earth System Sciences*, *21*(11), 3489–3508. https://doi.org/10.5194/nhess-21-3489-2021

Roger, J., Pelletier, B., Gusman, A., Power, W., Wang, X., Burbidge, D., & Duphil, M. (2023). Potential tsunami hazard of the Southern Vanuatu subduction zone: Tectonics, case study of the Matthew island tsunami of 10 February 2021 and implication in regional hazard assessment. *Natural Hazards and Earth System Sciences*, *23*(2), 393–414. https://doi.org/10.5194/nhess-23-393-2023

Romano, F., Molinari, I., Lorito, S., & Piatanesi, A. (2015). Source of the 6 February 2013 M_W = 8.0 Santa Cruz Islands Tsunami. *Natural Hazards and Earth System Sciences*, *15*(6), 1371–1379. https://doi.org/10.5194/nhess-15-1371-2015

Sahal, A., Pelletier, B., Chatelier, J., Lavigne, F., & Schindelé, F. (2010). A catalog of tsunamis in New Caledonia from 28 March 1875 to 30 September 2009. *Comptes Rendus Geoscience*, *342*(6), 434–447. https://doi.org/10.1016/j.crte.2010.01.013

Tanioka, Y., & Satake, K. (1996). Tsunami generated by horizontal displacement of ocean bottom. *Geophysical Research Letters*, *23*(8), 861–864. https://doi.org/10.1029/96GL00736

UNESCO-IOC. (2025). *Expert meeting on tsunami sources, hazards, risk and uncertainties associated with the Vanuatu, Solomon and New Britain subduction zones, Port Vila, Vanuatu, 14–17 May 2024*. UNESCO. Retrieved from https://unesdoc.unesco.org/ark:/48233/pf0000392448.locale=en

Yamazaki, Y., Bai, Y., Goo, L. L., Cheung, K. F., & Lay, T. (2023). Nonhydrostatic modeling of tsunamis from earthquake rupture to coastal impact. *Journal of Hydraulic Engineering*, *149*(9), 04023033. https://doi.org/10.1061/JHEND8.HYENG-13388

Yamazaki, Y., & Cheung, K. F. (2011). Shelf resonance and impact of near-field tsunami generated by the 2010 Chile earthquake. *Geophysical Research Letters*, *38*(12), L12605. https://doi.org/10.1029/2011GL047508

Yamazaki, Y., Cheung, K. F., & Kowalik, Z. (2011a). Depth-integrated, non-hydrostatic model with grid nesting for tsunami generation, propagation, and run-up. *International Journal for Numerical Methods in Fluids*, *67*(12), 2081–2107. https://doi.org/10.1002/fld.2485

Yamazaki, Y., Cheung, K. F., & Lay, T. (2018). A self-consistent fault slip model for the 2011 Tohoku earthquake and tsunami. *Journal of Geophysical Research: Solid Earth*, *123*(2), 1435–1458. https://doi.org/10.1002/2017JB014749

Yamazaki, Y., Kowalik, Z., & Cheung, K. F. (2009). Depth-integrated, non-hydrostatic model for wave breaking and run-up. *International Journal for Numerical Methods in Fluids*, *61*(5), 473–497. https://doi.org/10.1002/fld.1952

Yamazaki, Y., Lay, T., Cheung, K. F., Yue, H., & Kanamori, H. (2011). Modeling near-field tsunami observations to improve finite-fault slip models for the 11 March 2011 Tohoku earthquake. *Geophysical Research Letters*, *38*(7), L00G15. https://doi.org/10.1029/2011GL049130

Ye, L., Gong, W., Lay, T., Kanamori, H., & Chen, X. (2021). Shallow megathrust rupture during the 10 February 2021 M_W 7.7 Southeast Loyalty Islands earthquake sequence. *The Seismic Record*, *1*(3), 154–163. https://doi.org/10.1785/0320210035

Journal of Geophysical Research: Oceans

Supporting Information for

Tsunami Variability for the 2021 Megathrust and 2023 Outer Rise M_W 7.7 Earthquakes Southeast of the Loyalty Islands

William H. Robert[1,2], Yoshiki Yamazaki[1], Kwok Fai Cheung[1], and Thorne Lay[3]

[1]Department of Ocean and Resources Engineering, University of Hawaii at Manoa, Honolulu, Hawaii, USA

[2]Now at Stantec, Austin, Texas, USA

[3]Department of Earth and Planetary Sciences, University of California Santa Cruz, Santa Cruz, California, USA

Corresponding author: Kwok Fai Cheung (cheung@hawaii.edu)

Contents of this file

Figures S1 and S2
Data Sets S1 and S2: File structure and heading definitions
Movies S1 to S4: Captions and snapshots

Additional Supporting Information (Files uploaded separately)

Data Set S1: Source model for the 2021 M_W 7.7 thrust-faulting earthquake
Data Set S2: Source model for the 2023 M_W 7.7 normal-faulting earthquake
Movies S1: Near-field tsunami generated by the 2021 M_W 7.7 thrust-faulting earthquake
Movies S2: Near-field tsunami generated by the 2023 M_W 7.7 normal-faulting earthquake
Movies S3: Far-field tsunami generated by the 2021 M_W 7.7 thrust-faulting earthquake
Movies S4: Far-field tsunami generated by the 2023 M_W 7.7 normal-faulting earthquake

Introduction

The supporting information includes observed and synthetic seismic waveform comparisons, source model datasets, and tsunami animations for the 2021 thrust-faulting and 2023 normal-faulting M_W 7.7 earthquakes in the near and far fields.

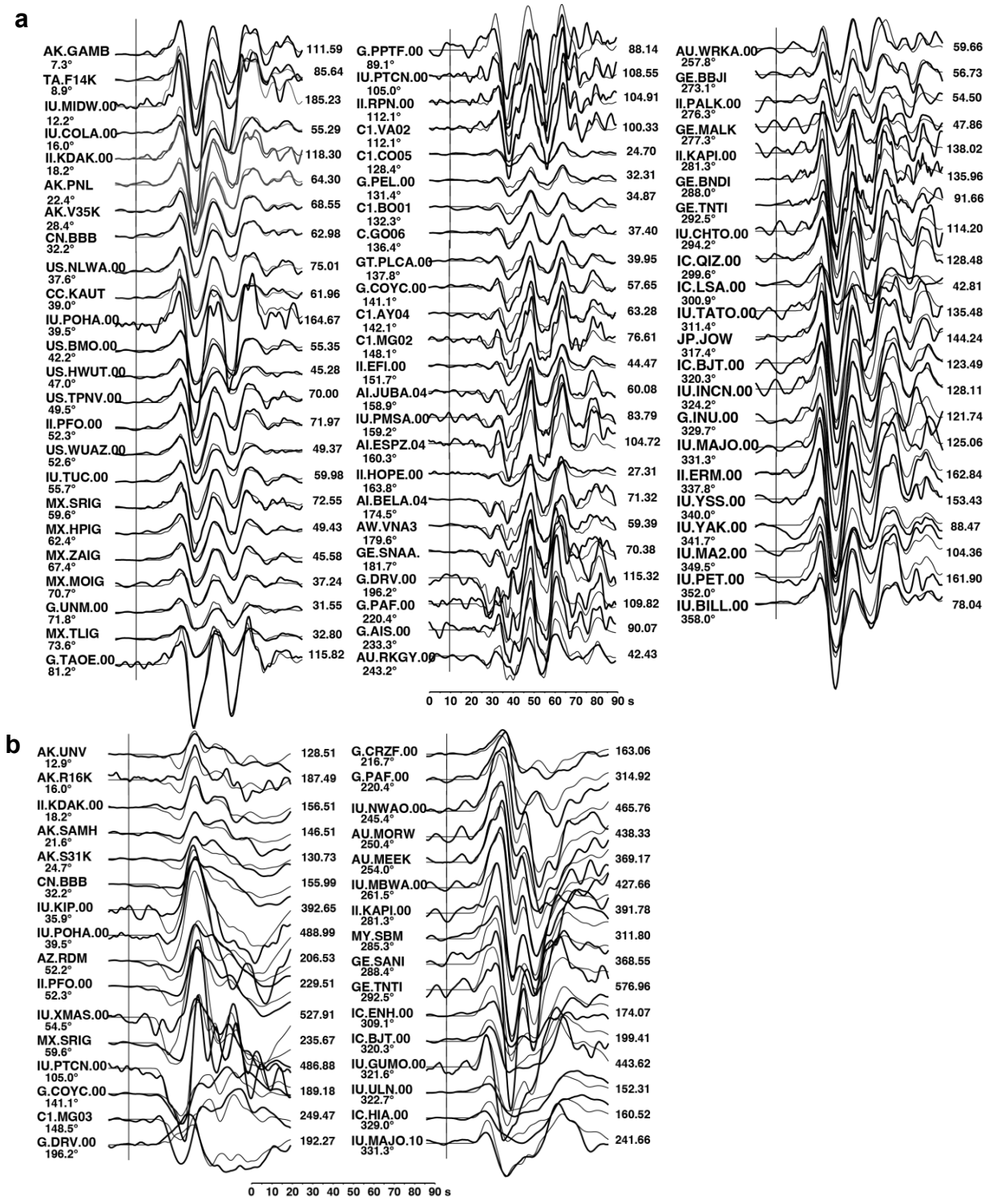

Figure S1. Comparison of observed (bold lines) and synthetic (light lines) teleseismic ground displacement data for the 2021 M_W 7.7 thrust-faulting earthquake. **a** *P* wave. **b** *SH* wave. The finite-fault model used for the synthetics is shown in Figure 3a. The observed and synthetic waveforms are all plotted on a common amplitude scale. The initial *P* and *SH* arrivals are aligned at 10 s. There is very small emergent motion in the first 10 s of the waveforms. The azimuth of each station is below the station name on the left side and the peak-to-peak amplitude of the observation is shown in microns on the right side of each trace pair. The model accounts for 85% of the power in the observed *P* and *SH* waveforms.

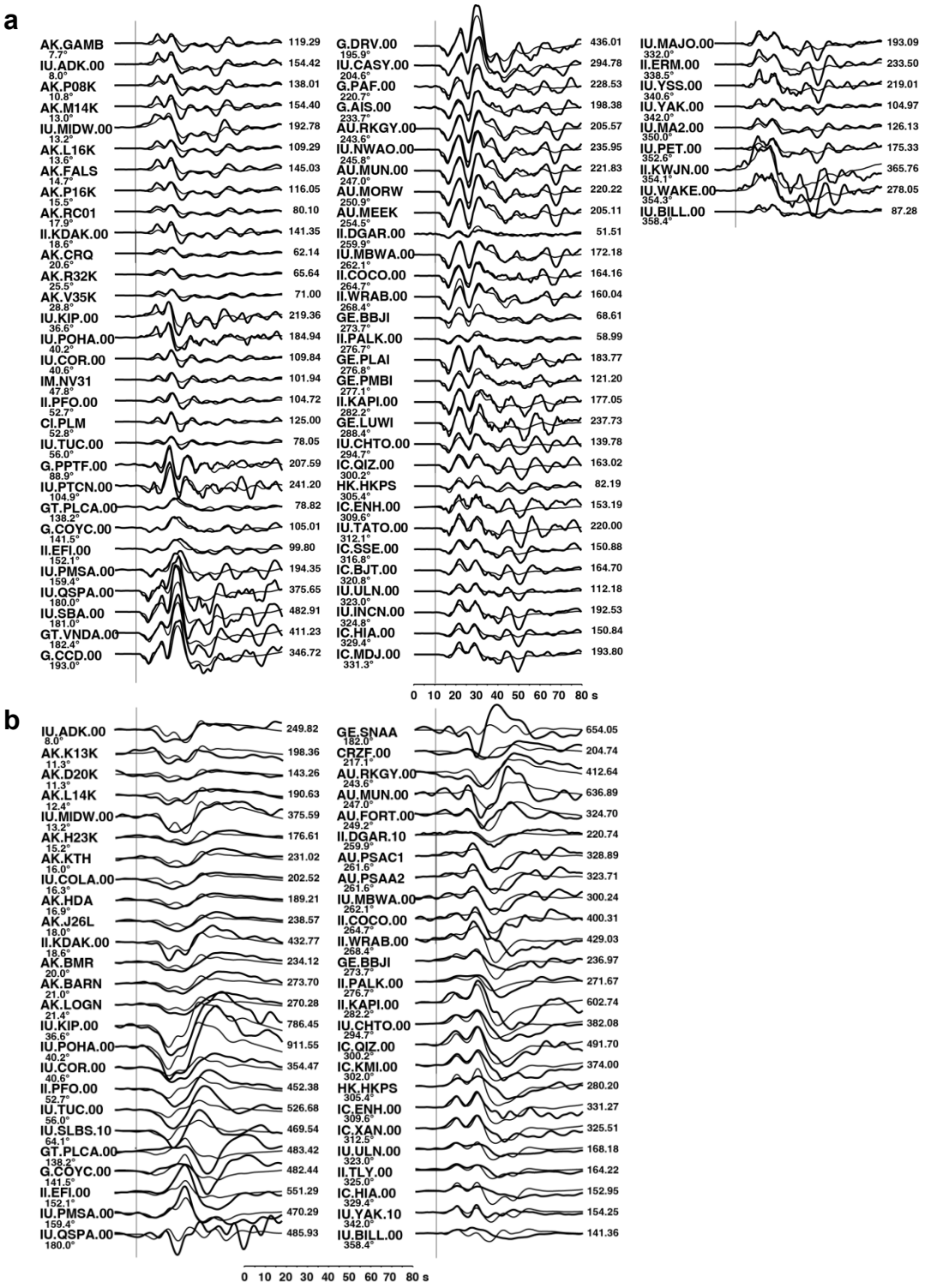

Figure S2. Comparison of observed (bold lines) and synthetic (light lines) teleseismic ground displacement data for the 2023 M_W 7.7 normal-faulting earthquake. **a** *P* wave. **b** *SH* wave. The finite-fault model used for the synthetics is shown in Figure 3b. The observed and synthetic waveforms are all plotted on a common amplitude scale. The initial *P* and *SH* arrivals are aligned at 10 s. The azimuth of each station is below the station name on the left side and the peak-to-peak amplitude of the observation is shown in microns on the right side of each trace pair. The model accounts for 66% of the power in the observed *P* and *SH* waveforms.

Data Sets S1 and S2. Text files with 12 columns and headings defined as

No = Subfault number

Tinit = Initiation time in second from earthquake origin time

Trise = Rise time in second

D0 = Slip in meters

lonR, LatR = Longitude and latitude in degree of the reference point* (N, E +ve; S, W -ve)

dR = Depth at reference point*

L, W = Subfault length and width in km

strike, dip, rake = Strike, dip, and rake angles in degree

*The reference point is at the southeast corner of subfaults for Data Set S1 and the northwest corner of subfaults for Data Set S2.

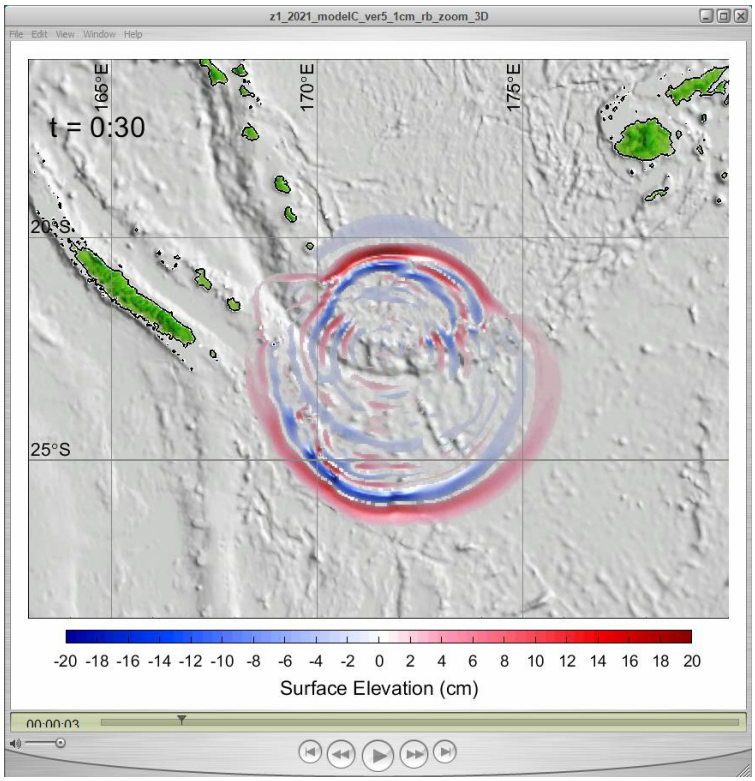

Movie 1. Near-field tsunami waves generated by the 2021 M_W 7.7 thrust-faulting earthquake. Elapsed time in hr:min after earthquake initiation time.

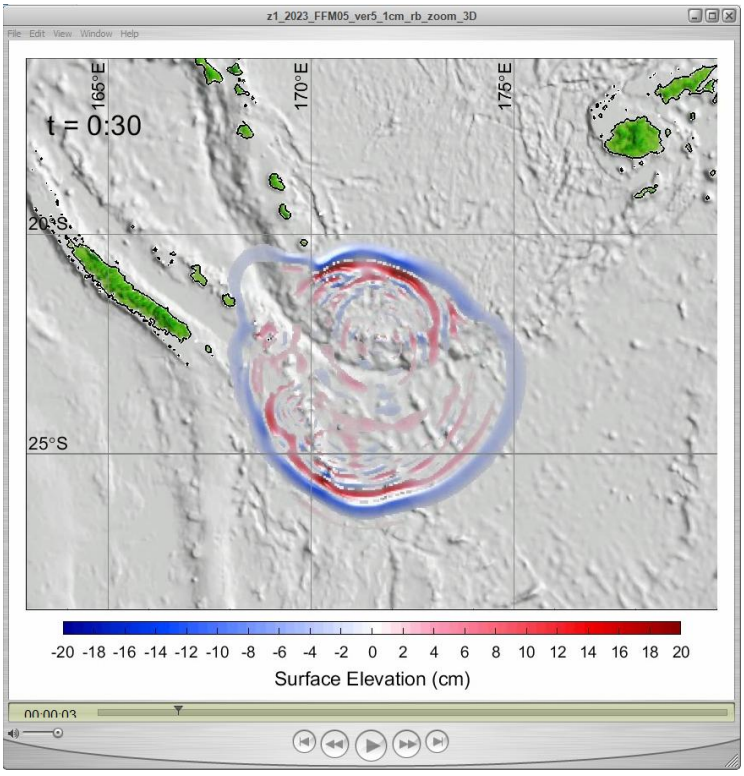

Movie 2. Near-field tsunami waves generated by the 2023 M_W 7.7 normal-faulting earthquake. Elapsed time in hr:min after earthquake initiation time.

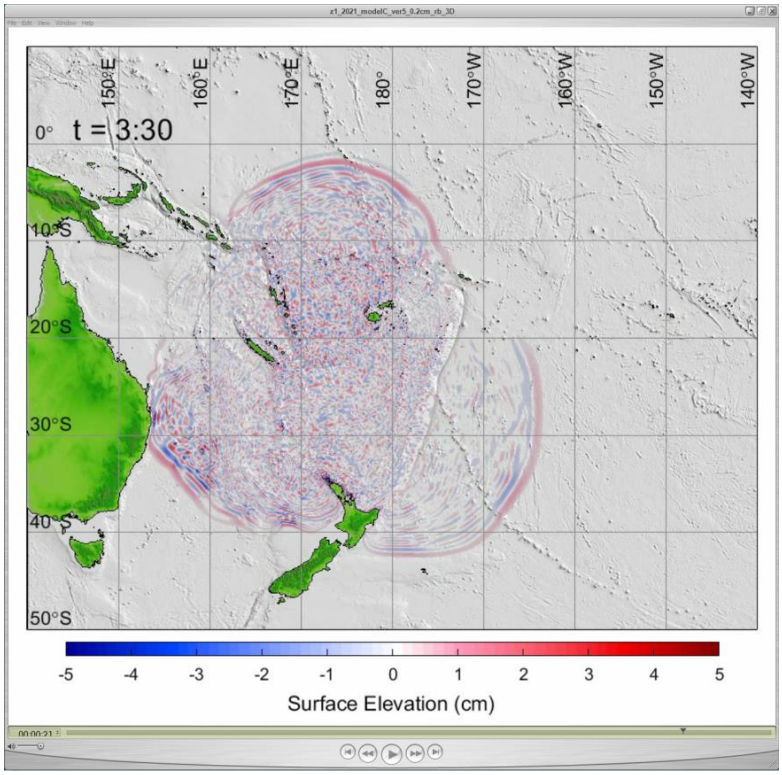

Movie 3. Far-field tsunami waves generated by the 2021 M_W 7.7 thrust-faulting earthquake. Elapsed time in hr:min after earthquake initiation time.

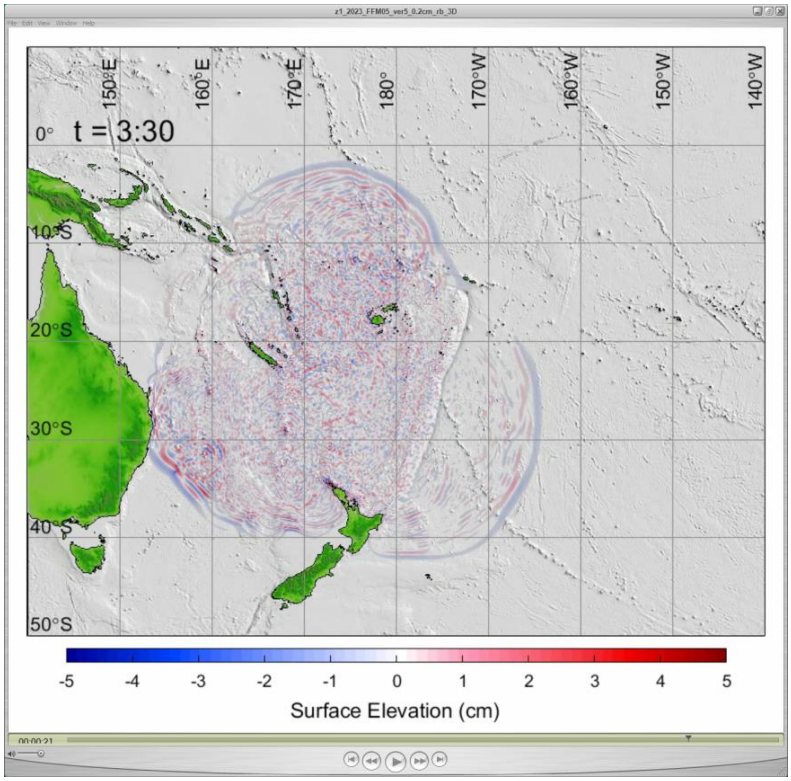

Movie 4. Far-field tsunami waves generated by the 2023 M_W 7.7 normal-faulting earthquake. Elapsed time in hr:min after earthquake initiation time.